

## Article

# Timing, Provenance, and Tectonic Implications of Ore-Hosting Metasedimentary Rocks in the Giant Liba Gold Deposit, West Qinling Belt, China

Peng-Cong Zhang<sup>1,2</sup>, Shan-Shan Li<sup>1,\*</sup>, Bo Liu<sup>2</sup>, Deng-Yang He<sup>1</sup>, Quan-Sheng Cai<sup>3</sup>,  
Germain Bishikwabo Kaningu<sup>1,4</sup> and Xin-Chun Sun<sup>5</sup>

- <sup>1</sup> State Key Laboratory of Geological Processes and Mineral Resources, School of Earth Sciences and Resources, China University of Geosciences, Beijing 100083, China; pengcongzhang0@gmail.com (P.-C.Z.); hedengyang1114@gmail.com (D.-Y.H.); germainkaningu@gmail.com (G.B.K.)
- <sup>2</sup> Key Laboratory of Ministry of Education on Safe Mining of Deep Metal Mines, Department of Geology, School of Resources and Civil Engineering, Northeastern University, Shenyang 110819, China; liubo@mail.neu.edu.cn
- <sup>3</sup> Zijin Mining Group Longnan Zijin Mining Co., Ltd., Longnan 746000, China; quanshengcailb@163.com
- <sup>4</sup> Department of Geology, Université Officielle de Bukavu, Bukavu 6210205, Democratic Republic of the Congo
- <sup>5</sup> Geological Survey of Gansu Province, Lanzhou 730000, China; gsddyzygb@126.com
- \* Correspondence: lishanshan199811@163.com



**Citation:** Zhang, P.-C.; Li, S.-S.; Liu, B.; He, D.-Y.; Cai, Q.-S.; Kaningu, G.B.; Sun, X.-C. Timing, Provenance, and Tectonic Implications of Ore-Hosting Metasedimentary Rocks in the Giant Liba Gold Deposit, West Qinling Belt, China. *Minerals* **2022**, *12*, 903. <https://doi.org/10.3390/min12070903>

Academic Editors: Kunfeng Qiu, Callum Hetherington and Yamirka Rojas-Agramonte

Received: 1 April 2022

Accepted: 28 June 2022

Published: 19 July 2022

**Publisher's Note:** MDPI stays neutral with regard to jurisdictional claims in published maps and institutional affiliations.



**Copyright:** © 2022 by the authors. Licensee MDPI, Basel, Switzerland. This article is an open access article distributed under the terms and conditions of the Creative Commons Attribution (CC BY) license (<https://creativecommons.org/licenses/by/4.0/>).

**Abstract:** The closure time of the Shangdan Ocean is critical for understanding the tectonic evolution of the Proto-Tethys Ocean. However, the proposed closure time was prolonged from Ordovician to Devonian. In the present study, detrital zircon from the metasedimentary rocks of the Liba Group in the West Qinling Belt was analyzed to constrain the closure time of the Shangdan Ocean. The three youngest grains from the Liba Group yield a maximum deposition age of  $418 \pm 13$  Ma, indicating the Middle Devonian deposition. Detrital zircon grains show two main U–Pb age peaks of 810 Ma and 440 Ma with  $\epsilon_{\text{Hf}(t)}$  values spanning from  $-24.3$  to  $+8.8$  and  $-6.3$  to  $+4.1$ , respectively, suggesting that the sediments of the Liba Group were derived from both the North and South Qinling Belts. The Lower Devonian in the South Qinling Belt shows similar provenance to the Liba Group, whereas sediments from the North Qinling Belt are absent in the Silurian strata of the South Qinling Belt. From Late Silurian to Early Devonian, the tectonic setting changed from subduction to collision. This evidence consistently suggests the disappearance of the Shangdan Ocean. The noticeable decrease in magmatism from 510–420 Ma to 420–390 Ma and the shrinking of  $\epsilon_{\text{Hf}(t)}$  values from  $-15.5$ – $+12.8$  to  $-8.4$ – $+4.2$  reveal that the Shangdan Ocean, as the eastmost embranchment of the Proto-Tethys Ocean, was closed at ca. 420 Ma.

**Keywords:** detrital zircon; Liba Group; Shangdan Ocean; tectonic evolution; West Qinling Belt

## 1. Introduction

The Qinling Belt, the eastmost branch of the Tethys domain, is divided into the North Qinling Belt and the South Qinling Belt by the Shangdan Suture Zone [1,2]. The Shangdan Ocean is the eastmost embranchment of the Proto-Tethys Ocean, which was closed during the Paleozoic and formed the Shangdan Suture Zone; therefore, the closure of the Shangdan Ocean recorded relevant information for understanding the tectonic evolution of the Proto-Tethys Ocean [3,4]. However, the closure time remains disputed, and several models have been proposed. Previous studies investigated S- and I-type granitoids, high Ba–Sr dioritic intrusions, and high-pressure and ultrahigh-pressure rocks, suggesting that the closure time of the Shangdan Ocean spanned from Ordovician to Silurian [5–7]. However, detrital zircon grains from the clastic rocks [8], adakitic granitoids [9], and mafic complex [10] indicate that the closure time can be constrained at Devonian.

Detrital zircon geochronology has been widely applied to investigate the orogenic event owing to the abundance of detrital zircon grains in the sedimentary rocks [11]. A routine application is to constrain the maximum depositional age of strata [12–15]. Moreover, the integration of the multiple-age populations and zircon Lu–Hf isotope is useful for tracing the provenance and tectonic evolution [8,11,16–18].

In the present study, representative metasedimentary rocks from the widely distributed Devonian Liba Group, which hosts the giant Liba gold deposit, was selected to investigate the geotectonic setting. Detrital zircon U–Pb geochronology and Lu–Hf isotope analyses were conducted to constrain the maximum depositional age and provenance of the Liba Group. Additionally, this study provides new insights into the tectonic evolution of the Proto-Tethys Ocean.

## 2. Geological Background

The Qinling Belt stretches across the Chinese mainland, extending several thousand kilometers from the Dabie-Sulu Orogen Belt in the east to the Kunlun Orogen Belt in the west [1,4,19–21]. It is tectonically bounded by the North China Block marked by the Lingbao–Lushan–Wuyang fault to the north and the South China Block marked by the Mianlue–Bashan–Xiangguang fault to the south (Figure 1a) [2,8,22]. Three ophiolitic suture zones were formed in the Qinling Belt from north to south, including the Neoproterozoic Kuanping, the Paleozoic Shangdan, and the Triassic Mianlue suture zones [2,3]. The Kuanping Suture Zone separates the southern margin of the North China Block from the North Qinling Belt and it is composed of the greenschist-facies ophiolitic suite [6,23–25]. The Shangdan Suture Zone that was formed by the collision between the North and South Qinling Belts is composed of Paleozoic ophiolites, subduction-related volcanics, and sedimentary rocks [26,27]. The Mianlue Suture Zone is the boundary between the South Qinling Belt and the South China Block, which mainly comprises dismembered ophiolitic sequences, ocean-island basalts, and island arc volcanic rocks [4,28].

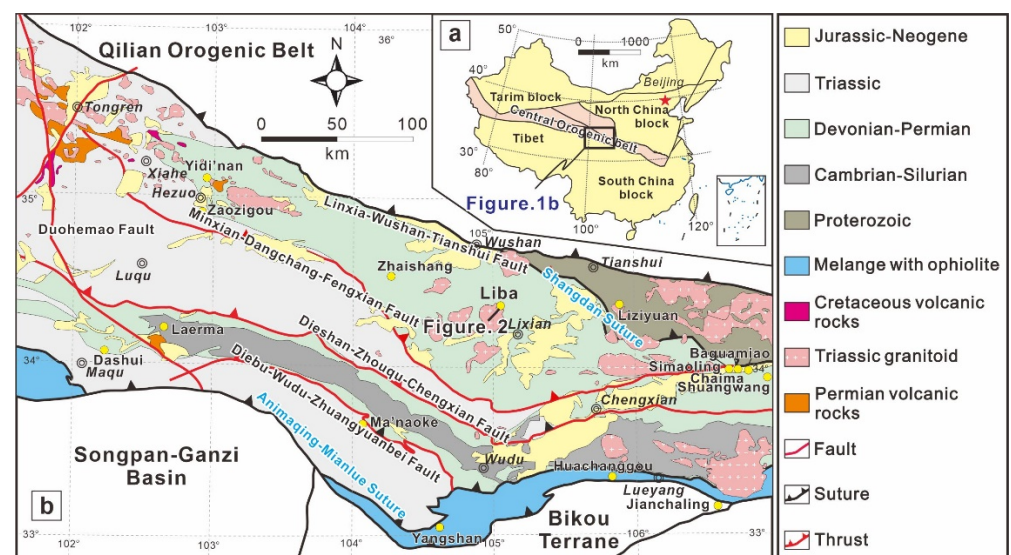


**Figure 1.** (a) Simplified map showing the location of the West Qinling Belt. (b) Geological map of the West Qinling Belt showing the major geological units (modified after [19]).

As the western segment of the Qinling Belt, the West Qinling Belt is contiguous to the East Qinling Belt and is bounded by the Huicheng basin or Foping dome [19,28–30]. In the West Qinling Belt, the Precambrian basement is overlain by the Phanerozoic sedimentary rocks and all the strata are intruded by the Triassic granitoid (Figure 1b) [31,32]. The ages of the Phanerozoic sedimentary rocks span from Ordovician to Neogene, including the Cambrian–Silurian limestones and shales, Devonian–Carboniferous clastic rocks with limestone interlayers, and Permian and Lower Triassic sandstones [8,31,33]. The Triassic

granitoid magmatism was mainly related to the continental collision between the South Qinling Belt and the South China Block with the formation of quartz diorites, quartz monzonites, granodiorites, and monzogranites [5,26,34,35]. Detailed geological mapping reveals that the Middle Devonian Liba Group was developed in the northern margin of the West Qinling Belt [32,36]. The Liba Group, also named the Shujiaba Group [32], is exposed between the Gaoqiao-Luoba fault to the south and the Shujiaba area to the north, which comprises marine metasedimentary rocks and hosts the giant Liba Gold deposit [32,36]. The Liba Group contains various rock types, including sericitic-chloritic slate, slate, meta-quartz sandstone, and siltstone (Figure 2) [37]. The major fault in the Liba gold deposit is the SW-dipping reverse F1 Fault (Figure 2). Numerous secondary W- to WNW-trending faults related to F1 are presented in the SW domain of the F1 Fault, hosting the major gold resources of the Liba gold deposit (Figure 2). The Liba Group is intruded by the Triassic monzogranite (Figure 2) [32].

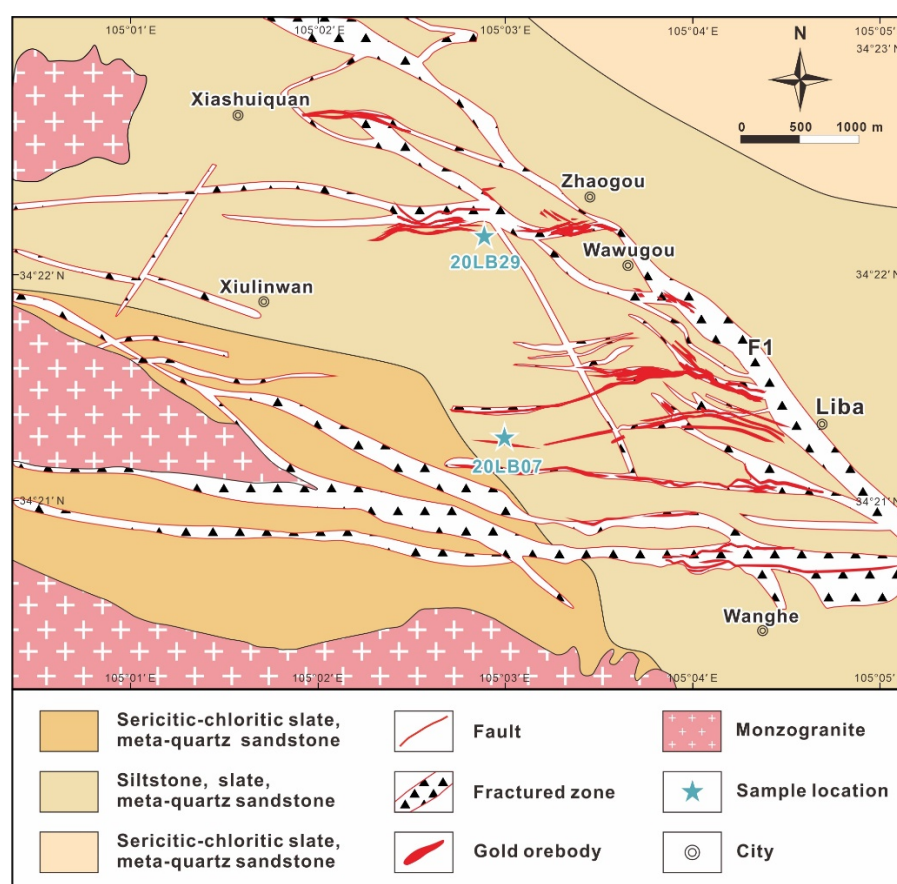


**Figure 2.** Geological map of the Liba gold deposit showing the major geological units and sample locations.

### 3. Samples and Methodology

#### 3.1. Sample Description

Two representative slate samples were collected from the Liba Group for zircon U–Pb and Lu–Hf analyses, namely, 20LB07 (34° 21′ 15″ N, 105° 03′ 13″ E) and 20LB29 (34° 22′ 14″ N, 105° 03′ 07″ E) (Figure 2). Detailed sample locations and hand specimen photographs are shown in Figures 2 and 3. The slates (20LB07, 20LB29) show dark gray and greenish colors and slaty structures (Figure 3) and consist of clay minerals and fine-grained quartz and muscovite (Figure 4a,b). Accessory minerals include zircon and pyrite (Figure 4c,d).

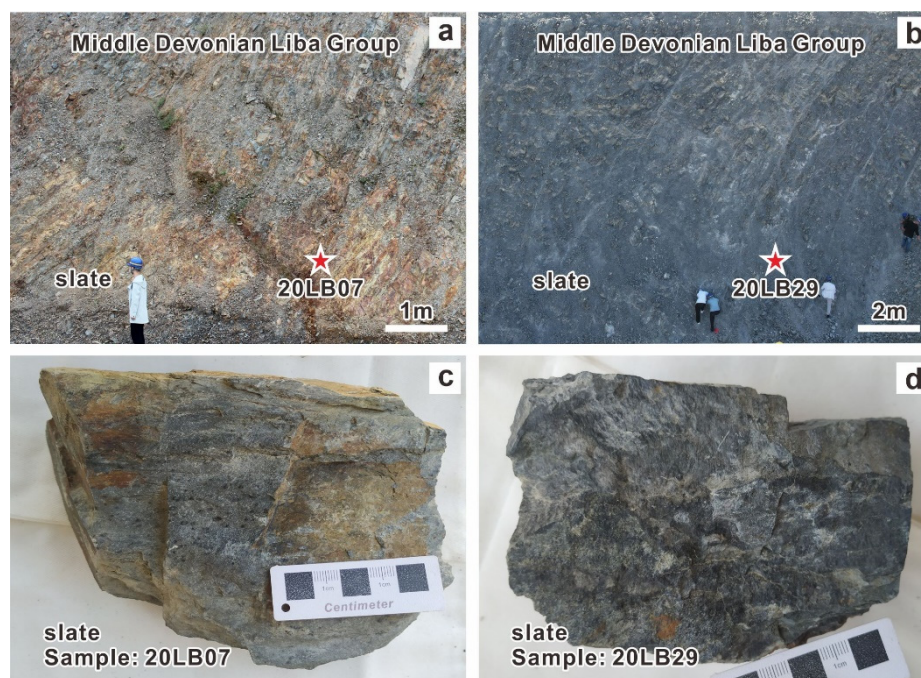


**Figure 3.** (a,b) Field photographs showing the slaty structure of the Middle Devonian Liba Group. (c,d) Hand specimens of the Middle Devonian Liba Group.

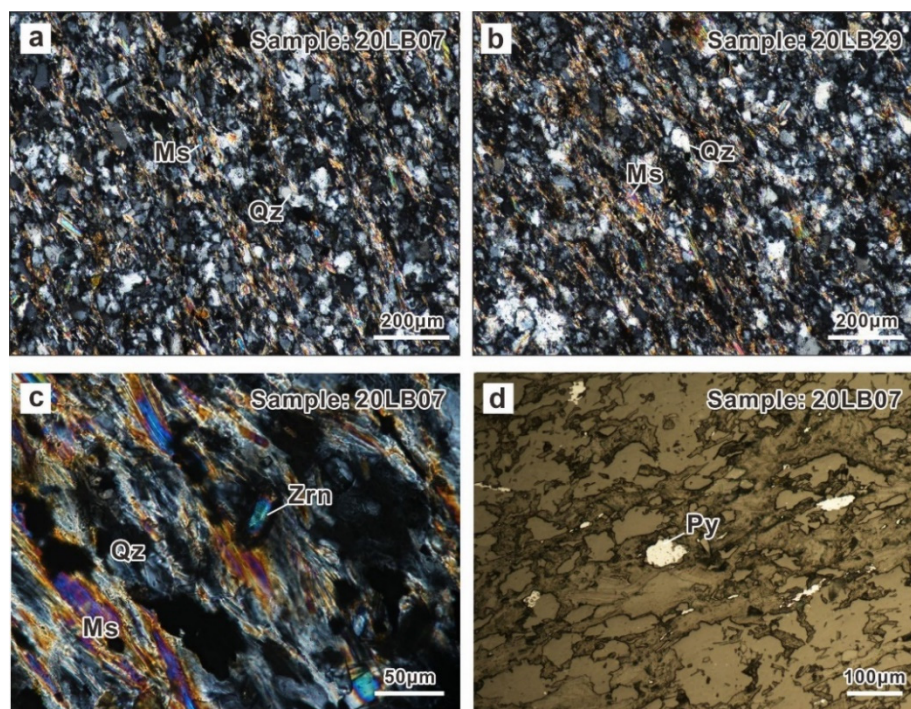


**Figure 4.** Photomicrographs showing mineral assemblages of the slates. (a–c) Transmitted cross-polarized light photomicrographs. (d) Reflected light photomicrograph. Ms—muscovite, Qz—quartz, Zrn—zircon, Py—pyrite.

### 3.2. Zircon U–Pb Dating

The separation of zircon grains was carried out at the Langfang Chengxin Geological Service Co., Hebei Province, China. The samples were first broken and crushed to 40–60 mesh, and then the standard heavy liquid and magnetic techniques were used to separate the zircon grains from the clastic grains. Detrital zircon grains without cracks and

inclusions were handpicked under a binocular microscope and mounted in epoxy resin. The zircon-grain-mounted samples were subsequently polished to nearly half the original thickness in order to expose the internal structures. The samples were then cleaned in an ultrasonic washer containing a 5% HNO<sub>3</sub> bath. Before analysis, cathodoluminescence (CL) images were obtained using a JXA8800 electron microscope at the Institute of Mineral Resources, Chinese Academy of Geological Sciences, Beijing, China, and all zircon grains were checked carefully to identify the internal structure.

Zircon U–Pb analyses were carried out using the LA-MC-ICP-MS at the Isotopic Laboratory, Tianjin Center, China Geological Survey. Laser sampling was performed using a Neptune double-focusing multiple-collector ICP-MS (Thermo Fisher Ltd., Waltham, MA, USA) attached to a NEW WAVE 193 nm-FX ArF Excimer laser ablation system (ESI Ltd., Fremont, CA, USA). The MC-ICP-MS is a double-focusing multi-collector ICP-MS. Two analyses of the standards followed every eight analyses to calibrate the data. The detailed analytical procedure of the laser ablation system, the ICP-MS instrument and the data reduction of zircon can be found in [38,39]. The common Pb corrections used the method of [40]. A laser beam diameter of 30 µm, a repetition rate of 8 Hz, and an energy density of 11 J/cm<sup>2</sup> were chosen for all U, Th and Pb analyses. Zircon 91500 [41] and zircon Plešovice [42] were used as standards. The NIST SRM 610 was used as external reference material and <sup>29</sup>Si as internal calibrant for calibration of U, Th and Pb concentrations. Probability density distribution curves and concordia diagrams of ages were plotted at the 2σ uncertainty level using the software DensityPlotter [43] and Isoplot software, respectively (version 3.75) [44]. The concordance was calculated for all data, with normal discordance <20% interpreted as geologically meaningful. Discordant data were excluded from the relative probability calculation. Ages of zircon grains inferior to 1.0 Ga are quoted using <sup>206</sup>Pb/<sup>238</sup>U ages, whereas older grains are based upon their <sup>207</sup>Pb/<sup>206</sup>Pb ages [45].

### 3.3. Zircon Lu–Hf Isotope Analysis

Zircon Lu–Hf isotopic analyses were conducted on the same spots or textural domains as analogous zircon U–Pb analysis. Hafnium isotopic compositions were determined with a Thermo Finnigan Neptune MC-ICP-MS system coupled to a New Wave UP193 nm laser ablation system at the Isotopic Laboratory, Tianjin Center, China Geological Survey. A laser beam diameter of 50 µm and a laser repetition rate of 11 Hz at 100 mJ were used for ablating zircon with helium as the carrier gas for the ablated aerosol. Details about the analytical procedures and the instrument operating conditions for Lu–Hf isotope analyses follow those described in [38]. Zircon GJ-1 was used as the reference standard with a weighted mean <sup>176</sup>Hf/<sup>177</sup>Hf ratio of 0.282004 ± 24 (2σ) during routine analyses, which is significantly consistent with the recommended <sup>176</sup>Hf/<sup>177</sup>Hf ratios of 0.282015 ± 19 (2σ) [46].

## 4. Results

### 4.1. Detrital Zircon U–Pb Geochronology

Detrital zircon morphology is illustrated in Figure 5. The two slate samples (20LB07 and 20LB29) show similar zircon morphologies. Cathodoluminescence (CL) images show that most zircon grains from the Liba Group have crystal faces and oscillatory zoning. Some grains exhibit irregular sector zoning and banded zoning textures. The rest of the grains are homogeneous with low to high luminescence. Zircon grains from sample 20LB07 have lengths of 30–120 µm; among them, 70% of the grains show small size (30–40 µm), while 30% have lengths of 60–120 µm (Figure 5a). Zircon grains from sample 20LB29 display lengths of 40–70 µm and length/width ratios ranging from 2:1 to 1:1 (Figure 5b).

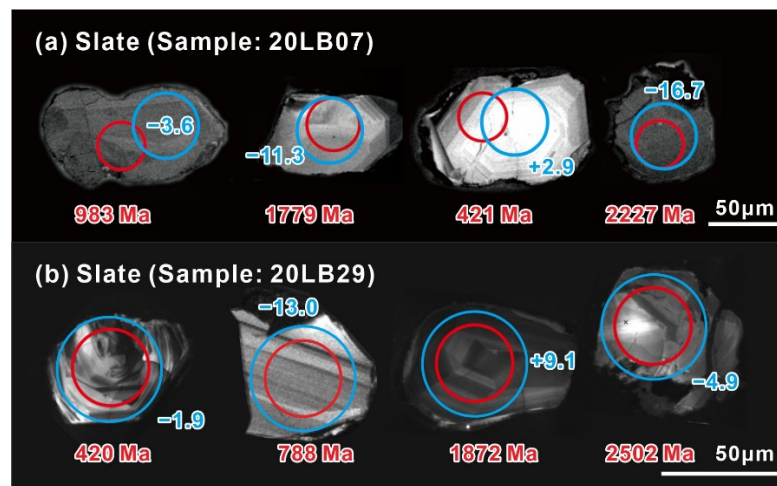


**Figure 5.** Representative cathodoluminescence (CL) images showing the morphologies and internal textures of zircon grains from the Middle Devonian Liba Group. (a) Sample 20LB07; (b) Sample 20LB29.

Detrital zircon U–Pb ages from the Liba Group are shown in Figure 6 and Table 1, the two samples display similar age spectra. Eighty detrital zircon grains from sample 20LB07 were analyzed, among which seventy show high concordance (concordance > 80%) (Figure 6a), yielding ages ranging from 2912 Ma to 256 Ma. The relative probability density curve plotted by the Density Plotter software [43] yields two major peaks at 803 Ma and 433 Ma and a minor peak at 1.2 Ga (Figure 6b). Forty zircon grains were analyzed from sample 20LB29, and most of them show high concordance ( $n = 34$ , concordance > 80%) (Figure 6c). The relative probability density curve shows a main peak at 826 Ma, followed by a second peak at 733 Ma and a minor peak at 1.8 Ga (Figure 6d). The U–Pb age distributions of the two samples are presented in Figure 7a; four age populations are highlighted, including Archean–Mesoproterozoic (2912–1045 Ma), Neoproterozoic (993–631 Ma), and Phanerozoic (517–133 Ma).

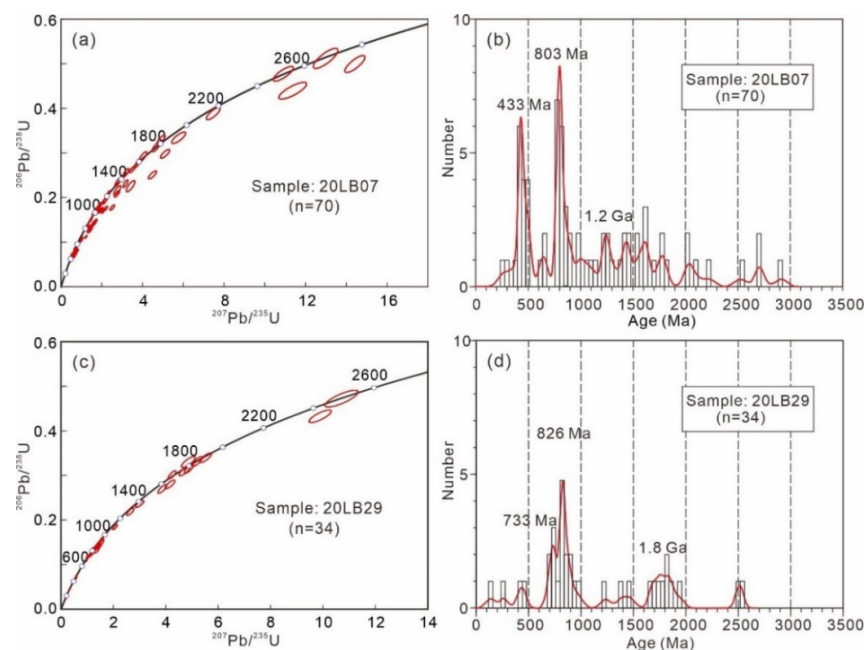


**Figure 6.** (a,c) Detrital zircon U–Pb concordia diagrams of the Middle Devonian Liba Group slate samples. (b,d) Detrital zircon probability density distribution curves of the Middle Devonian Liba Group slate samples.

#### 4.2. Lu–Hf Isotopic Composition

Twenty-seven spots of the analyzed U–Pb domains or the same textural domains of the zircon grains from the two samples of the Liba Group were analyzed for Lu–Hf isotopic compositions, and the result is shown in Figure 7b and Table 2. Detrital zircon grains of the 2.5–1.0 Ga group are characterized by variable  $\epsilon_{\text{Hf}(t)}$  values spanning from  $-16.7$  to  $+9.1$  and  $T_{\text{DM2}}$  age of 3.8–1.7 Ga. Zircon grains clustering around 800 Ma show  $\epsilon_{\text{Hf}(t)}$  values from  $-24.3$  to  $+10.4$  and  $T_{\text{DM2}}$  age of 3.1–1.2 Ga. The 430 Ma population group has  $\epsilon_{\text{Hf}(t)}$  values between  $-6.3$  and  $+5.5$  with a median of  $+2.9$  and  $T_{\text{DM2}}$  age of 1.8–1.1 Ga.

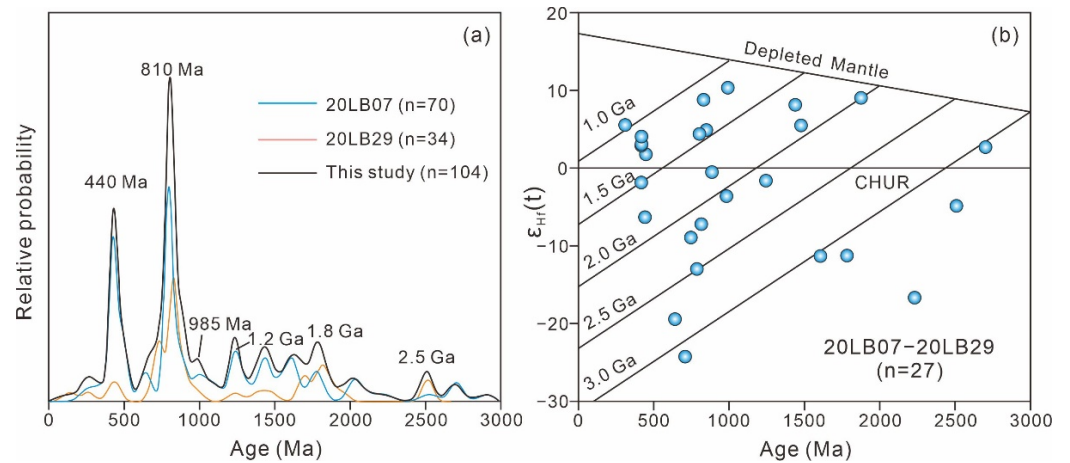


**Figure 7.** (a) Detrital zircon U–Pb age spectra of sample 20LB07 and 20LB29 from the Liba Group. (b) Detrital zircon  $\epsilon_{\text{Hf}(t)}$  values versus U–Pb age diagram of the Liba Group.

**Table 1.** Zircon LA-ICP-MS U–Pb data of the Liba Group. Ages of zircon grains (<1.0 Ga) are quoted using  $^{206}\text{Pb}/^{238}\text{U}$  ages, whereas older grains are based on their  $^{207}\text{Pb}/^{206}\text{Pb}$  ages. Zircon ages with low concordance (<80%) were excluded.

Sample No.	Elemental Data (ppm)		Th/U	Isotopic Ratios						Age (Ma)						Concordance (%)	
	U	Th		$^{207}\text{Pb}/^{206}\text{Pb}$		$^{207}\text{Pb}/^{235}\text{U}$		$^{206}\text{Pb}/^{238}\text{U}$		$^{207}\text{Pb}/^{206}\text{Pb}$		$^{207}\text{Pb}/^{235}\text{U}$		$^{206}\text{Pb}/^{238}\text{U}$			Best age
				Ratio	1 $\sigma$	Ratio	1 $\sigma$	Ratio	1 $\sigma$	Age	1 $\sigma$	Age	1 $\sigma$	Age	1 $\sigma$		
20LB07: Slate																	
20LB07-01	102	84	0.82	0.0581	0.0014	0.5360	0.0147	0.0675	0.0011	533	52	436	10	421	7	421	97
20LB07-02	114	92	0.81	0.0564	0.0018	0.5193	0.0173	0.0679	0.0013	469	70	425	12	423	8	423	100
20LB07-03	131	91	0.70	0.0692	0.0012	1.2322	0.0265	0.1300	0.0022	906	37	815	12	788	12	788	97
20LB07-04	401	232	0.58	0.0701	0.0015	1.2600	0.0298	0.1311	0.0028	931	43	828	13	794	16	794	96
20LB07-05	390	177	0.45	0.0715	0.0009	1.6211	0.0340	0.1647	0.0025	973	26	978	13	983	14	983	100
20LB07-06	1277	690	0.54	0.0819	0.0011	2.3223	0.0364	0.2068	0.0030	1244	25	1219	11	1212	16	1244	99
20LB07-07	108	115	1.07	0.1106	0.0016	3.4190	0.0884	0.2248	0.0051	1810	27	1509	20	1307	27	1810	87
20LB07-08	225	64	0.29	0.0874	0.0013	2.7867	0.0555	0.2334	0.0037	1369	28	1352	15	1352	20	1369	100
20LB07-09	533	231	0.43	0.1399	0.0017	7.4783	0.1398	0.3882	0.0057	2227	21	2170	17	2115	26	2227	95
20LB07-10	78	25	0.32	0.1667	0.0023	10.9107	0.2016	0.4776	0.0068	2525	24	2516	17	2517	30	2525	100
20LB07-11	457	204	0.45	0.1845	0.0023	12.9854	0.2478	0.5122	0.0092	2694	20	2679	18	2666	39	2694	99
20LB07-12	3071	2247	0.73	0.0734	0.0017	0.5820	0.0128	0.0574	0.0010	1025	46	466	8	360	6	360	77
20LB07-13	2885	4083	1.42	0.0631	0.0011	0.5209	0.0135	0.0594	0.0010	712	37	426	9	372	6	372	87
20LB07-14	1878	1521	0.81	0.0808	0.0021	0.6766	0.0181	0.0603	0.0009	1216	50	525	11	377	5	377	72
20LB07-15	348	304	0.87	0.0727	0.0013	0.6621	0.0154	0.0662	0.0010	1005	37	516	9	413	6	413	80
20LB07-16	135	131	0.97	0.0604	0.0019	0.5801	0.0210	0.0693	0.0012	619	66	465	13	432	7	432	93
20LB07-17	1339	677	0.51	0.0742	0.0016	0.7380	0.0152	0.0717	0.0009	1046	44	561	9	446	5	446	80
20LB07-18	1275	1968	1.54	0.0597	0.0012	0.5980	0.0110	0.0727	0.0010	591	45	476	7	452	6	452	95
20LB07-19	407	276	0.68	0.0717	0.0016	0.7901	0.0239	0.0795	0.0011	977	45	591	14	493	6	493	83
20LB07-20	511	318	0.62	0.0745	0.0014	0.8221	0.0165	0.0797	0.0012	1056	38	609	9	495	7	495	81
20LB07-21	1040	339	0.33	0.0667	0.0009	0.7738	0.0139	0.0832	0.0009	829	27	582	8	515	5	515	89
20LB07-22	1004	338	0.34	0.0579	0.0009	0.6670	0.0131	0.0835	0.0011	525	35	519	8	517	7	517	100
20LB07-23	472	264	0.56	0.0873	0.0025	1.0384	0.0224	0.0861	0.0015	1368	54	723	11	533	9	533	74
20LB07-24	503	74	0.15	0.0701	0.0011	0.9893	0.0192	0.1028	0.0016	931	33	698	10	631	9	631	90
20LB07-25	560	417	0.74	0.0700	0.0013	1.0119	0.0275	0.1049	0.0023	929	39	710	14	643	13	643	91
20LB07-26	317	173	0.55	0.0766	0.0015	1.4095	0.0276	0.1333	0.0013	1110	39	893	12	807	8	807	90
20LB07-27	283	179	0.63	0.0687	0.0011	1.2825	0.0245	0.1353	0.0017	890	33	838	11	818	9	818	98
20LB07-28	427	287	0.67	0.0958	0.0018	1.8416	0.0347	0.1380	0.0016	1544	36	1060	12	833	9	833	79
20LB07-29	433	334	0.77	0.0842	0.0017	1.6374	0.0409	0.1411	0.0023	1297	38	985	16	851	13	851	86
20LB07-30	1295	526	0.41	0.0841	0.0013	1.6959	0.0347	0.1460	0.0017	1295	30	1007	13	878	10	878	87
20LB07-31	803	92	0.11	0.1091	0.0037	2.1624	0.0632	0.1461	0.0045	1784	62	1169	20	879	25	879	75

Table 1. Cont.

Sample No.	Elemental Data (ppm)			Isotopic Ratios						Age (Ma)						Concordance (%)	
	U	Th	Th/U	$^{207}\text{Pb}/^{206}\text{Pb}$		$^{207}\text{Pb}/^{235}\text{U}$		$^{206}\text{Pb}/^{238}\text{U}$		$^{207}\text{Pb}/^{206}\text{Pb}$		$^{207}\text{Pb}/^{235}\text{U}$		$^{206}\text{Pb}/^{238}\text{U}$			Best age
				Ratio	1 $\sigma$	Ratio	1 $\sigma$	Ratio	1 $\sigma$	Age	1 $\sigma$	Age	1 $\sigma$	Age	1 $\sigma$		
20LB07-32	816	141	0.17	0.0713	0.0008	1.4782	0.0223	0.1498	0.0016	967	24	921	9	900	9	900	98
20LB07-33	373	174	0.47	0.0711	0.0010	1.4741	0.0228	0.1504	0.0017	961	29	920	9	903	9	903	98
20LB07-34	1058	123	0.12	0.1188	0.0024	2.6146	0.0534	0.1592	0.0018	1938	36	1305	15	952	10	952	73
20LB07-35	175	80	0.46	0.0780	0.0017	1.7762	0.0395	0.1665	0.0025	1146	44	1037	14	993	14	993	96
20LB07-36	544	77	0.14	0.0778	0.0016	1.8087	0.0424	0.1697	0.0029	1141	41	1049	15	1010	16	1141	96
20LB07-37	250	272	1.09	0.0845	0.0014	1.9866	0.0436	0.1698	0.0019	1304	32	1111	15	1011	10	1304	91
20LB07-38	504	93	0.18	0.0832	0.0015	1.9578	0.0384	0.1706	0.0025	1273	36	1101	13	1015	14	1273	92
20LB07-39	427	249	0.58	0.0909	0.0012	2.2063	0.0374	0.1745	0.0021	1445	24	1183	12	1037	12	1445	88
20LB07-40	383	132	0.34	0.1035	0.0016	2.5222	0.0476	0.1765	0.0025	1687	29	1278	14	1048	14	1687	82
20LB07-41	849	80	0.09	0.0757	0.0010	1.9232	0.0353	0.1825	0.0023	1088	25	1089	12	1081	13	1088	99
20LB07-42	850	386	0.45	0.0812	0.0018	2.1572	0.0424	0.1916	0.0030	1227	44	1167	14	1130	16	1227	97
20LB07-43	453	270	0.60	0.0815	0.0014	2.1887	0.0484	0.1943	0.0027	1233	33	1177	15	1145	15	1233	97
20LB07-44	689	48	0.07	0.0959	0.0017	2.7530	0.0535	0.2075	0.0030	1546	34	1343	14	1216	16	1546	91
20LB07-45	387	252	0.65	0.0925	0.0013	2.7674	0.0708	0.2155	0.0042	1478	27	1347	19	1258	22	1478	93
20LB07-46	600	378	0.63	0.1814	0.0022	6.2493	0.1074	0.2484	0.0026	2666	20	2011	15	1430	14	2666	71
20LB07-47	625	264	0.42	0.1298	0.0022	4.4920	0.0821	0.2499	0.0037	2095	29	1729	15	1438	19	2095	83
20LB07-48	198	162	0.82	0.0963	0.0013	3.4970	0.0574	0.2619	0.0028	1553	25	1527	13	1500	14	1553	98
20LB07-49	378	372	0.98	0.1268	0.0022	4.7102	0.0978	0.2670	0.0037	2054	31	1769	17	1525	19	2054	74
20LB07-50	113	188	1.67	0.1354	0.0023	5.2682	0.1038	0.2806	0.0037	2169	30	1864	17	1594	18	2169	73
20LB07-51	447	386	0.86	0.0999	0.0013	4.0249	0.0783	0.2911	0.0045	1623	25	1639	16	1647	23	1623	101
20LB07-52	1166	1035	0.89	0.1239	0.0018	5.1110	0.0929	0.2975	0.0041	2014	26	1838	15	1679	20	2014	83
20LB07-53	323	86	0.27	0.1078	0.0013	4.6699	0.0802	0.3128	0.0044	1763	22	1762	14	1755	22	1763	100
20LB07-54	118	76	0.65	0.1256	0.0026	5.7808	0.1407	0.3335	0.0053	2037	37	1944	21	1855	26	2037	91
20LB07-55	296	177	0.60	0.1871	0.0017	9.1863	0.1493	0.3548	0.0049	2716	15	2357	15	1957	23	2716	72
20LB07-56	361	161	0.45	0.1868	0.0025	11.3731	0.2791	0.4394	0.0077	2714	22	2554	23	2348	35	2714	87
20LB07-57	410	194	0.47	0.0620	0.0012	0.3412	0.0067	0.0405	0.0008	674	41	298	5	256	5	256	86
20LB07-58	337	488	1.45	0.0523	0.0010	0.3552	0.0072	0.0493	0.0008	300	43	309	5	310	5	310	101
20LB07-59	707	478	0.68	0.0600	0.0012	0.5592	0.0121	0.0677	0.0010	604	43	451	8	423	6	423	94
20LB07-60	185	150	0.81	0.0554	0.0014	0.5388	0.0155	0.0705	0.0010	428	58	438	10	439	6	439	100
20LB07-61	638	489	0.77	0.0549	0.0008	0.5387	0.0112	0.0715	0.0012	409	33	438	7	445	7	445	102
20LB07-62	302	135	0.45	0.0648	0.0014	0.6778	0.0150	0.0763	0.0013	768	45	525	9	474	7	474	90
20LB07-63	482	444	0.92	0.0807	0.0014	1.2263	0.0208	0.1104	0.0013	1215	34	813	9	675	8	675	83
20LB07-64	264	268	1.02	0.0822	0.0015	1.4290	0.0270	0.1263	0.0013	1250	36	901	11	767	7	767	85

Table 1. Cont.

Sample No.	Elemental Data (ppm)			Isotopic Ratios						Age (Ma)						Concordance (%)	
	U	Th	Th/U	$^{207}\text{Pb}/^{206}\text{Pb}$		$^{207}\text{Pb}/^{235}\text{U}$		$^{206}\text{Pb}/^{238}\text{U}$		$^{207}\text{Pb}/^{206}\text{Pb}$		$^{207}\text{Pb}/^{235}\text{U}$		$^{206}\text{Pb}/^{238}\text{U}$			Best age
				Ratio	1 $\sigma$	Ratio	1 $\sigma$	Ratio	1 $\sigma$	Age	1 $\sigma$	Age	1 $\sigma$	Age	1 $\sigma$		
20LB07-65	151	111	0.74	0.0827	0.0030	1.4274	0.0515	0.1267	0.0029	1262	71	900	22	769	16	769	85
20LB07-66	420	218	0.52	0.0707	0.0009	1.2423	0.0151	0.1281	0.0016	950	25	820	7	777	9	777	95
20LB07-67	257	261	1.01	0.0693	0.0014	1.2557	0.0274	0.1312	0.0021	909	42	826	12	795	12	795	96
20LB07-68	448	241	0.54	0.0704	0.0010	1.2733	0.0202	0.1314	0.0018	941	30	834	9	796	11	796	95
20LB07-69	455	155	0.34	0.0820	0.0013	1.5090	0.0292	0.1336	0.0020	1246	31	934	12	808	12	808	87
20LB07-70	81	51	0.63	0.0695	0.0014	1.2837	0.0278	0.1343	0.0017	914	42	839	12	812	9	812	97
20LB07-71	431	264	0.61	0.0698	0.0008	1.2867	0.0203	0.1344	0.0021	922	25	840	9	813	12	813	97
20LB07-72	305	126	0.41	0.0813	0.0014	1.5496	0.0343	0.1378	0.0022	1229	33	950	14	832	12	832	88
20LB07-73	492	242	0.49	0.0819	0.0008	1.5701	0.0256	0.1397	0.0023	1244	20	958	10	843	13	843	88
20LB07-74	876	422	0.48	0.0894	0.0011	2.0798	0.0292	0.1698	0.0024	1413	23	1142	10	1011	13	1413	88
20LB07-75	637	413	0.65	0.0741	0.0008	1.7796	0.0309	0.1740	0.0029	1045	23	1038	11	1034	16	1045	100
20LB07-76	812	121	0.15	0.1001	0.0014	3.1671	0.0489	0.2305	0.0035	1625	25	1449	12	1337	18	1625	92
20LB07-77	671	417	0.62	0.0906	0.0016	3.1871	0.0577	0.2549	0.0039	1438	34	1454	14	1464	20	1438	101
20LB07-78	443	118	0.27	0.0989	0.0009	3.7643	0.0504	0.2766	0.0041	1604	17	1585	11	1574	20	1604	98
20LB07-79	82	96	1.17	0.1088	0.0019	4.9086	0.0805	0.3290	0.0042	1779	32	1804	14	1833	20	1779	103
20LB07-80	355	239	0.67	0.2108	0.0021	14.4226	0.2018	0.4995	0.0078	2912	16	2778	13	2612	33	2912	90
20LB29: Slate																	
20LB29-01	872	1313	1.51	0.0918	0.0017	1.5331	0.0286	0.1213	0.0015	1465	35	944	11	738	8	738	78
20LB29-02	5	9	2.00	0.4948	0.0227	38.0579	2.1680	0.5646	0.0225	4226	68	3721	56	2886	93	4226	68
20LB29-03	459	408	0.89	0.0557	0.0019	0.1591	0.0052	0.0209	0.0004	443	76	150	5	133	2	133	89
20LB29-04	568	478	0.84	0.0691	0.0011	1.1726	0.0236	0.1230	0.0018	902	27	788	11	748	11	748	95
20LB29-05	549	679	1.24	0.0579	0.0009	0.5782	0.0103	0.0725	0.0008	524	31	463	7	451	5	451	97
20LB29-06	258	285	1.11	0.0730	0.0017	1.4219	0.0360	0.1411	0.0016	1014	46	898	15	851	9	851	95
20LB29-07	365	229	0.63	0.0702	0.0011	1.3438	0.0232	0.1391	0.0017	1000	31	865	10	840	10	840	97
20LB29-08	297	262	0.88	0.1026	0.0013	4.2357	0.0615	0.3000	0.0038	1672	22	1681	12	1691	19	1672	101
20LB29-09	882	263	0.30	0.0824	0.0015	0.9203	0.0336	0.0794	0.0022	1255	34	663	18	492	13	492	74
20LB29-10	250	200	0.80	0.1107	0.0014	4.7181	0.0873	0.3091	0.0046	1810	24	1770	16	1736	23	1810	96
20LB29-11	325	173	0.53	0.0816	0.0012	2.0511	0.0358	0.1826	0.0024	1235	28	1133	12	1081	13	1235	95
20LB29-12	533	855	1.61	0.0606	0.0010	0.5622	0.0105	0.0673	0.0008	633	35	453	7	420	5	420	93
20LB29-13	214	255	1.19	0.0693	0.0017	1.3111	0.0353	0.1373	0.0019	909	55	851	16	829	11	829	97
20LB29-14	1638	1821	1.11	0.0670	0.0008	1.1022	0.0209	0.1192	0.0019	837	26	754	10	726	11	726	96
20LB29-15	157	204	1.30	0.1182	0.0016	5.5178	0.0916	0.3383	0.0044	1944	29	1903	14	1879	21	1944	97

Table 1. Cont.

Sample No.	Elemental Data (ppm)		Th/U	Isotopic Ratios						Age (Ma)						Concordance (%)	
				$^{207}\text{Pb}/^{206}\text{Pb}$		$^{207}\text{Pb}/^{235}\text{U}$		$^{206}\text{Pb}/^{238}\text{U}$		$^{207}\text{Pb}/^{206}\text{Pb}$		$^{207}\text{Pb}/^{235}\text{U}$		$^{206}\text{Pb}/^{238}\text{U}$			Best age
	U	Th		Ratio	1 $\sigma$	Ratio	1 $\sigma$	Ratio	1 $\sigma$	Age	1 $\sigma$	Age	1 $\sigma$	Age	1 $\sigma$		
20LB29-16	6	5	0.82	0.3826	0.0149	21.1843	0.8772	0.4082	0.0107	3842	58	3147	40	2207	49	3842	57
20LB29-17	429	200	0.47	0.0729	0.0011	1.6604	0.0294	0.1653	0.0023	1013	30	994	11	986	13	986	99
20LB29-18	302	157	0.52	0.1144	0.0015	5.2032	0.0809	0.3303	0.0045	1872	24	1853	13	1840	22	1872	98
20LB29-19	228	243	1.07	0.0704	0.0014	1.2899	0.0300	0.1329	0.0019	943	38	841	13	804	11	804	96
20LB29-20	79	65	0.82	0.1345	0.0051	1.2245	0.0440	0.0672	0.0012	2157	61	812	20	419	8	419	52
20LB29-21	353	121	0.34	0.1081	0.0015	4.1589	0.0772	0.2785	0.0040	1765	26	1666	15	1584	20	1765	90
20LB29-22	368	285	0.77	0.1666	0.0027	9.9043	0.1728	0.4319	0.0058	2524	26	2426	16	2314	26	2524	92
20LB29-23	1420	34	0.02	0.0710	0.0009	1.4358	0.0201	0.1465	0.0016	967	25	904	8	881	9	881	97
20LB29-24	569	270	0.48	0.0722	0.0010	1.5429	0.0253	0.1547	0.0019	991	29	948	10	927	10	927	98
20LB29-25	142	187	1.31	0.0657	0.0016	1.2043	0.0286	0.1331	0.0018	798	55	803	13	805	10	805	100
20LB29-26	64	77	1.19	0.1069	0.0019	4.8597	0.1090	0.3289	0.0050	1748	33	1795	19	1833	24	1748	105
20LB29-27	548	104	0.19	0.0754	0.0018	1.3571	0.0387	0.1303	0.0025	1080	48	871	17	789	15	789	91
20LB29-28	205	265	1.29	0.0882	0.0016	2.6383	0.0565	0.2169	0.0034	1387	36	1311	16	1265	18	1387	96
20LB29-29	87	3	0.03	0.0732	0.0023	1.3913	0.0519	0.1367	0.0023	969	61	885	22	826	13	826	93
20LB29-30	657	576	0.88	0.1040	0.0014	3.8653	0.0704	0.2684	0.0039	1698	24	1606	15	1533	20	1698	90
20LB29-31	1308	452	0.35	0.0628	0.0009	0.9702	0.0171	0.1118	0.0016	702	30	689	9	683	10	683	99
20LB29-32	216	368	1.70	0.0640	0.0017	1.0283	0.0293	0.1164	0.0017	739	59	718	15	710	10	710	99
20LB29-33	563	569	1.01	0.0676	0.0013	1.1472	0.0253	0.1228	0.0020	852	118	776	12	747	12	747	96
20LB29-34	153	120	0.78	0.0924	0.0017	2.9943	0.0654	0.2344	0.0032	1476	35	1406	17	1357	17	1476	97
20LB29-35	315	239	0.76	0.0685	0.0012	1.3066	0.0265	0.1378	0.0017	898	32	849	12	832	10	832	98
20LB29-36	780	1153	1.48	0.1444	0.0018	5.7725	0.0936	0.2893	0.0040	2281	19	1942	14	1638	20	2281	72
20LB29-37	820	634	0.77	0.1126	0.0011	4.8861	0.0736	0.3141	0.0042	1839	19	1800	13	1761	21	1839	96
20LB29-38	814	236	0.29	0.0756	0.0011	1.5420	0.0334	0.1475	0.0026	1083	35	947	13	887	15	887	94
20LB29-39	385	199	0.52	0.0530	0.0013	0.3050	0.0084	0.0417	0.0006	309	55	270	7	263	3	263	97
20LB29-40	86	169	1.98	0.1643	0.0024	10.7247	0.2599	0.4715	0.0077	2502	25	2500	23	2490	34	2502	100

Table 2. Zircon Lu–Hf data of the Liba Group.

Sample No.	$^{176}\text{Yb}/^{177}\text{Hf}$		$^{176}\text{Lu}/^{177}\text{Hf}$		$^{176}\text{Hf}/^{177}\text{Hf}$		Age (Ma)	$\varepsilon\text{Hf}(0)$	$\varepsilon\text{Hf}(t)$	$T_{\text{DM1}}$ (Ma)	$T_{\text{DM2}}$ (Ma)	$f\text{L}_{\text{u}}/\text{Hf}$
	Radio	$2\sigma$	Radio	$2\sigma$	Radio	$2\sigma$						
20LB07-1	0.013074	0.000145	0.000540	0.000005	0.282596	0.000020	421	−6.22	2.90	917	1220	−0.98
20LB07-2	0.008366	0.000034	0.000363	0.000001	0.282627	0.000015	423	−5.13	4.08	870	1147	−0.99
20LB07-3	0.028609	0.000065	0.001087	0.000001	0.281928	0.000021	788	−29.83	−13.02	1864	2497	−0.97
20LB07-5	0.021034	0.000055	0.000802	0.000002	0.282070	0.000013	983	−24.83	−3.62	1655	2059	−0.98
20LB07-6	0.053580	0.000094	0.001954	0.000002	0.281992	0.000013	1244	−27.59	−1.63	1818	2134	−0.94
20LB07-9	0.016293	0.000036	0.000628	0.000001	0.280919	0.000016	2227	−65.54	−16.72	3208	3803	−0.98
20LB07-11	0.025443	0.000277	0.001062	0.000010	0.281190	0.000016	2694	−55.93	2.71	2876	2983	−0.97
20LB07-25	0.045395	0.000387	0.001811	0.000014	0.281842	0.000031	643	−32.88	−19.50	2022	2790	−0.95
20LB07-27	0.047238	0.000766	0.001608	0.000024	0.282082	0.000028	818	−24.42	−7.24	1675	2159	−0.95
20LB07-35	0.028579	0.000064	0.001321	0.000003	0.282468	0.000028	993	−10.76	10.36	1118	1191	−0.96
20LB07-58	0.053395	0.000165	0.002103	0.000008	0.282747	0.000028	310	−0.88	5.51	737	969	−0.94
20LB07-59	0.062902	0.000261	0.002439	0.000012	0.282615	0.000124	423	−5.55	3.08	937	1210	−0.93
20LB07-61	0.030130	0.000181	0.001098	0.000006	0.282325	0.000021	445	−15.80	−6.33	1312	1821	−0.97
20LB07-77	0.042669	0.000416	0.001581	0.000016	0.282142	0.000020	1438	−22.30	8.16	1589	1674	−0.95
20LB07-78	0.028591	0.000181	0.000995	0.000005	0.281473	0.000026	1604	−45.92	−11.34	2485	3007	−0.97
20LB07-79	0.021656	0.000074	0.000794	0.000002	0.281360	0.000022	1779	−49.94	−11.28	2627	3135	−0.98
20LB29-4	0.068266	0.000193	0.002565	0.000009	0.282088	0.000066	748	−24.18	−8.96	1709	2213	−0.92
20LB29-5	0.020610	0.000120	0.000782	0.000004	0.282548	0.000022	451	−7.92	1.78	990	1314	−0.98
20LB29-6	0.013123	0.000284	0.000450	0.000009	0.282386	0.000029	851	−13.65	4.90	1206	1424	−0.99
20LB29-12	0.034350	0.000303	0.001380	0.000013	0.282469	0.000019	420	−10.72	−1.86	1118	1520	−0.96
20LB29-18	0.027344	0.000131	0.001159	0.000004	0.281888	0.000015	1872	−31.27	9.07	1924	1955	−0.97
20LB29-25	0.056838	0.000224	0.002216	0.000009	0.282427	0.000022	805	−12.19	4.41	1204	1419	−0.93
20LB29-32	0.008442	0.000272	0.000330	0.000010	0.281647	0.000014	710	−39.79	−24.32	2209	3139	−0.99
20LB29-34	0.043098	0.000743	0.001565	0.000024	0.282043	0.000023	1476	−25.76	5.51	1726	1868	−0.95
20LB29-35	0.067060	0.000936	0.002222	0.000031	0.282536	0.000037	832	−8.36	8.81	1047	1163	−0.93
20LB29-38	0.028617	0.000091	0.001044	0.000004	0.282220	0.000014	887	−19.50	−0.52	1456	1792	−0.97
20LB29-40	0.029522	0.000262	0.000997	0.000008	0.281095	0.000016	2502	−59.29	−4.86	3000	3295	−0.97

## 5. Discussion

### 5.1. Timing of Deposition of the Liba Group

Detrital zircon ages from the two metasedimentary rocks of the Liba Group are combined to discuss the depositional age owing to their similar age spectra (Figures 5 and 6). Most of the zircon grains show high concordance (>95%) and Th/U ratios of 0.10–1.98 (Figure 8), which, together with the well-developed oscillatory zoning in CL images (Figure 4), indicates the magmatic origin [47,48]. Except the three low-Th/U-ratio grains (21LB29-23: 0.02, 21LB29-29: 0.03, and 21LB07-44: 0.07) (Table 1), the high Th/U ratios of magmatic grains were further discussed. The present study follows the method of “mean age of the youngest two or more grains that overlap in age at  $1\sigma$ ”, which yields a weighted mean age of  $418 \pm 13$  Ma ( $n = 3$ , MSWD = 0.111), representing the maximum depositional age of the Liba Group [14]. The calculated youngest age indicates that the deposition of the Liba Group formed after ca. 418 Ma. Combined with the stratigraphic successions of the upper layers of the Late Devonian paleosporangium fossils and the bottom layers of the early Middle Devonian coral fossils [36,49–51], the deposition of the Liba Group is constrained in the Middle Devonian.

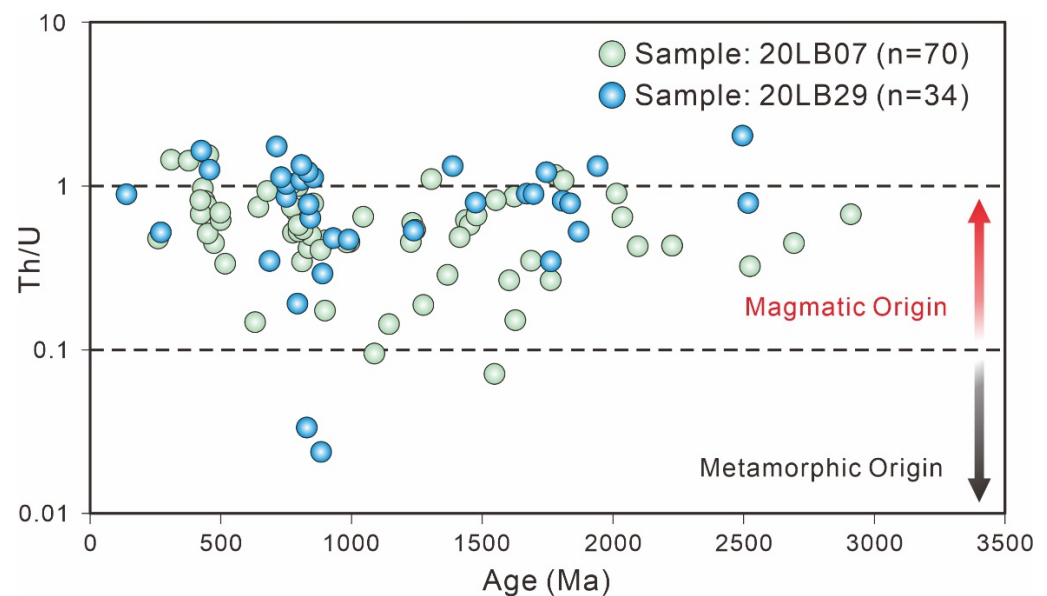


**Figure 8.** Th/U ratios of the detrital zircon from the Middle Devonian Liba Group.

### 5.2. Provenance of the Liba Group

The detrital zircon grains of the Liba Group were presumably sourced from the North Qinling Belt, South Qinling Belt, North China Block, and South China Block (Figure 1a). The U–Pb age and  $\epsilon\text{Hf}(t)$  value of the detrital zircon grains from the Liba group and magmatic zircon from surrounding orogenic belts are compared (Figure 9) to trace the provenance of the Liba Group. Detrital zircon U–Pb ages indicate that the metasedimentary rocks of the Liba Group predominantly deposited during the Phanerozoic (440 Ma) and Neoproterozoic (810 Ma) and minimally were during the Archean–Mesoproterozoic (1.2 Ga, 1.8 Ga, and 2.5 Ga) (Figure 9a). The variable age populations of the Liba Group are similar to the zircon distributions of neighboring orogenic belts, suggesting mixed sources (Figure 9a).

The Phanerozoic detrital zircon grains are subhedral to angular (Figure 5), whose ages range from 500 to 400 Ma with a dominant peak at 440 Ma (Figure 9a), implying a short transport distance [14,17]. The Phanerozoic ages are highly consistent with the early Paleozoic magmatism in the North Qinling Belt (Figure 9). The major peak of ca. 440 Ma coincides with the ca. 445 Ma magmatism of the Liuxiangping, Huichizi, and Zaoyuan granitic plutons [7]. The dominant positive and minor negative  $\epsilon\text{Hf}(t)$  values from the Liba group generally overlap the available zircon  $\epsilon\text{Hf}(t)$  values (−20 to +13) from granitoid and

gabbro intrusions in the North Qinling Belt (Figure 9b) [27,53]. Consequently, the early Paleozoic magmatic rocks from the North Qinling Belt might be the main source of the Phanerozoic zircon grains of the Liba Group.

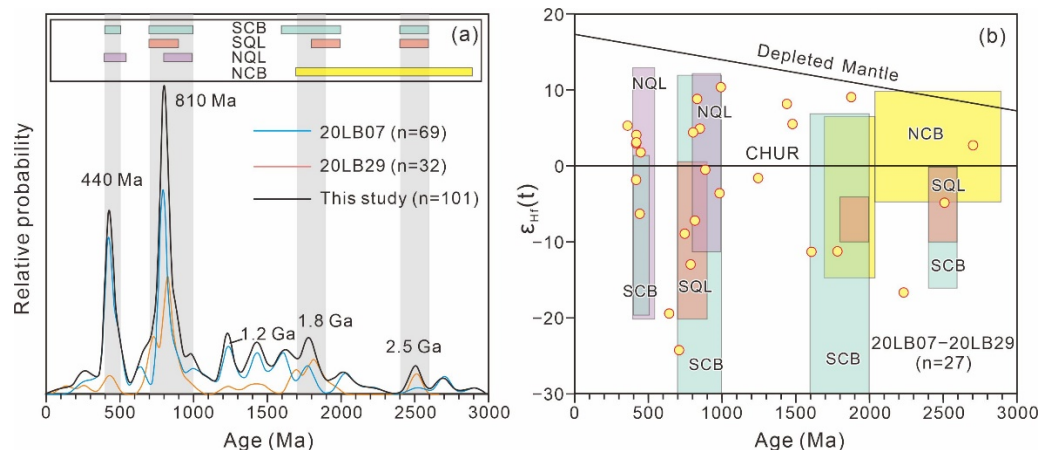


**Figure 9.** (a) Detrital zircon U–Pb age spectra of the Middle Devonian Liba Group and magmatic zircon distributions from neighboring orogenic belts. (b) Detrital zircon  $\epsilon_{\text{Hf}}(t)$  values versus U–Pb age diagram of the Liba Group. Data of North China Block, South China Block, North Qinling Belt and South Qinling Belt are from [27,52–55]. NCB = North China Block, NQB = North Qinling Belt, SQB = South Qinling Belt, SCB = South China Block.

The dominant Neoproterozoic grains display ages ranging from 1000 Ma to 700 Ma with a major peak at 810 Ma and a minor peak at 985 Ma (Figure 9a). In the present study, the major peak of ca. 810 Ma closely matches with the age distribution of the South Qinling Belt and South China Block (Figure 9a). The South Qinling Belt is characterized by significant Neoproterozoic zircon ranging from 1000 to 700 Ma with an age peak at 820 Ma, which was defined by the Yaolinghe volcanic rocks (808–746 Ma), Mihunzhen plutons (885–737 Ma) and Liuba granitic intrusions (868–794 Ma) [27,52]. Additionally, the Neoproterozoic ages (ca. 900–700 Ma) are also widely reported in the South China Block, including the Bikou, Hannan, and Micanshan massif [27,53]. Furthermore, the  $\epsilon_{\text{Hf}}(t)$  values (−24.3 to +8.8, Figure 9b) from the ca. 900–700 Ma group of this study generally overlap the zircon  $\epsilon_{\text{Hf}}(t)$  values (−30.2 to +17.7) from the magmatic rocks in the South China Block (Figure 9b; [27]) and the negative  $\epsilon_{\text{Hf}}(t)$  values from the South Qinling Belt (Figure 10; [27]), which indicates that the two regions could be the potential provenance for the middle Neoproterozoic zircon grains. Moreover, considering that the South China Block and South Qinling Belt were separated by the Mianlue Ocean during the Devonian [3,56], the Neoproterozoic detrital zircon grains (ca. 810 Ma) were probably sourced from the South Qinling Belt. However, the age population of 1000–900 Ma shows different provenance from the ca. 810 Ma population. In contrast to the absence of the Neoproterozoic (ca. 1000–900 Ma) magmatic events in the South China Block or South Qinling Belt, the Neoproterozoic (ca. 1000–900 Ma) magmatism was reported in the North Qinling Belt, represented by the exposed Dehe granite (943–964 Ma), Niujaoshan granite (929–959 Ma), and the Tianshui granitoid (915–978 Ma) [27,57]. Thus, the Neoproterozoic (1000–900 Ma) zircon grains of the Liba Group were likely sourced from the North Qinling Belt.

The ca. 1.5–1.0 Ga, ca. 1.9–1.7 Ga, and ca. 2.5 Ga age groups were also observed in the present study (Figure 9a). Mesoproterozoic detrital zircon grains whose ages range from 1.5 to 1.0 Ga with a peak at 1.2 Ga are only reported in the Qinling Group and Kuanping Group in the North Qinling Belt [53], indicating that the Mesoproterozoic detrital zircon grains were sourced from the North Qinling Belt. The Archean–Paleoproterozoic gneiss and amphibolite from the North China Block show zircon ages of 3.5–3.1 Ga and 2.8–1.7 Ga with peaks at 2.6–2.4 Ga and 2.0–1.7 Ga [58–60], and their  $\epsilon_{\text{Hf}}(t)$  values scatter from −10 to +5 and −15 to +10, respectively [54,61]. The South China Block also displays

age populations of 2.6–2.4 Ga and 2.0–1.8 Ga with  $\epsilon\text{Hf}_t$  values from  $-16$  to  $+0$  and  $-30$  to  $+7$ , respectively [52]. The ages and  $\epsilon\text{Hf}_t$  values from the detrital zircon in this study closely match with those of zircon grains from the North China Block and South China Block (Figure 9); thus, the Archean–Paleoproterozoic detrital zircon grains of the Liba Group mainly originated from the North China Block and South China Block.

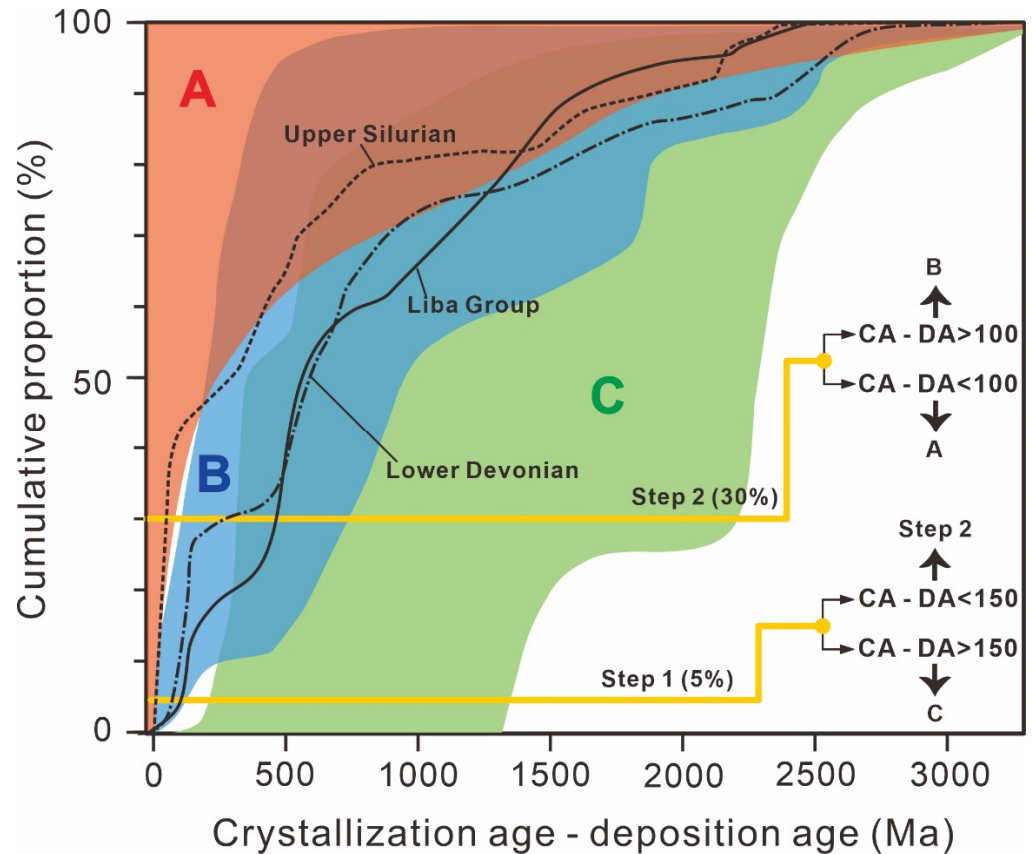


**Figure 10.** Detrital zircon U–Pb age cumulative probability distributions. Summary plot of the general fields for convergent (A: orange field), collisional (B: blue field), and extensional basins (C: green field). Extensional setting shows  $\text{CA-DA} > 150$  Ma in 5% of the youngest zircon grains (step 1), convergent setting shows  $\text{CA-DA} < 100$  Ma in 30% of the youngest zircon grains (step 2), and collisional setting shows  $\text{CA-DA} < 150$  Ma and  $\text{CA-DA} > 100$  Ma in 5% and 30% of the youngest zircon population, respectively (modified after [17]).

### 5.3. Closure Time of the Shangdan Ocean

The widely distributed Middle Devonian Liba Group in the South Qinling Belt received abundant Phanerozoic sediments from the North Qinling Belt, suggesting that the Shangdan Ocean between the North and South Qinling Belts had closed in the Middle Devonian. The difference between the crystallization and deposition ages (CA-DA) of the detrital zircon grains can be demonstrated (Figure 10) by the method of [17]. Overall, a significant proportion of the youngest detrital zircon ( $\text{CA-DA} < 150$  Ma at 5% and  $\text{CA-DA} > 100$  Ma at 30% of the zircon population), combined with the overlapping feature of the cumulative proportional curves of the Liba Group in the B (blue) area (Figure 10), consistently supports that the Liba group was formed in a collisional setting. Consequently, the Shangdan Ocean presumably closed in the Middle Devonian during the deposition of the Liba Group.

Based on the early Paleozoic (ca. 450 Ma) and Neoproterozoic (900–700 Ma) age groups and their negative  $\epsilon\text{Hf}_t$  values, previous studies suggest that the Silurian strata in South Qinling Belt received sediments from the South China Block and Ordovician detritus from the South Qinling Belt without the contribution of the North Qinling Belt

and the North China Block (Figure 11a,c) [52,62,63]. However, the Lower Devonian in the South Qinling Belt dominantly shows early Paleozoic ages (ca. 450 Ma) with positive  $\varepsilon_{\text{Hf}(t)}$  values and new Neoproterozoic zircon ages (1000–900 Ma) (Figure 11b,d), suggesting that the North Qinling Belt is the major source [62,64,65]. Furthermore, the detrital zircon grains from the Middle Devonian [66] and Middle–Upper Devonian strata [8,27,65–70] show similar provenance to the Lower Devonian (Figure 11b,d), indicating that the tectonic setting remains unchanged. The apparent provenance difference between the Silurian and Lower Devonian strata might be the result of the collision between the North and South Qinling Belts [2]. The cumulative proportion curves also show tectonic settings changed from convergent to collision settings from Upper Silurian to Lower Devonian (Figure 10). Among the youngest zircon grains, the Upper Silurian samples present 42% (more than 30%) detrital grains that have CA-DA < 100 Ma, while lower Devonian samples present 5% zircon grains that show CA-DA < 150 Ma and 30% zircon grains that have CA-DA > 100 Ma, suggesting that the Upper Silurian and Lower Devonian strata formed in convergent and collision settings, respectively (Figure 12). In the South Qinling Belt, the Silurian strata did not originate from the North Qinling Belt, while abundant Lower Devonian sediments were sourced from the North Qinling Belt. Combined with the change of the tectonic setting from subduction to collision, the closure time of the Shangdan Ocean is constrained between Late Silurian and Early Devonian.

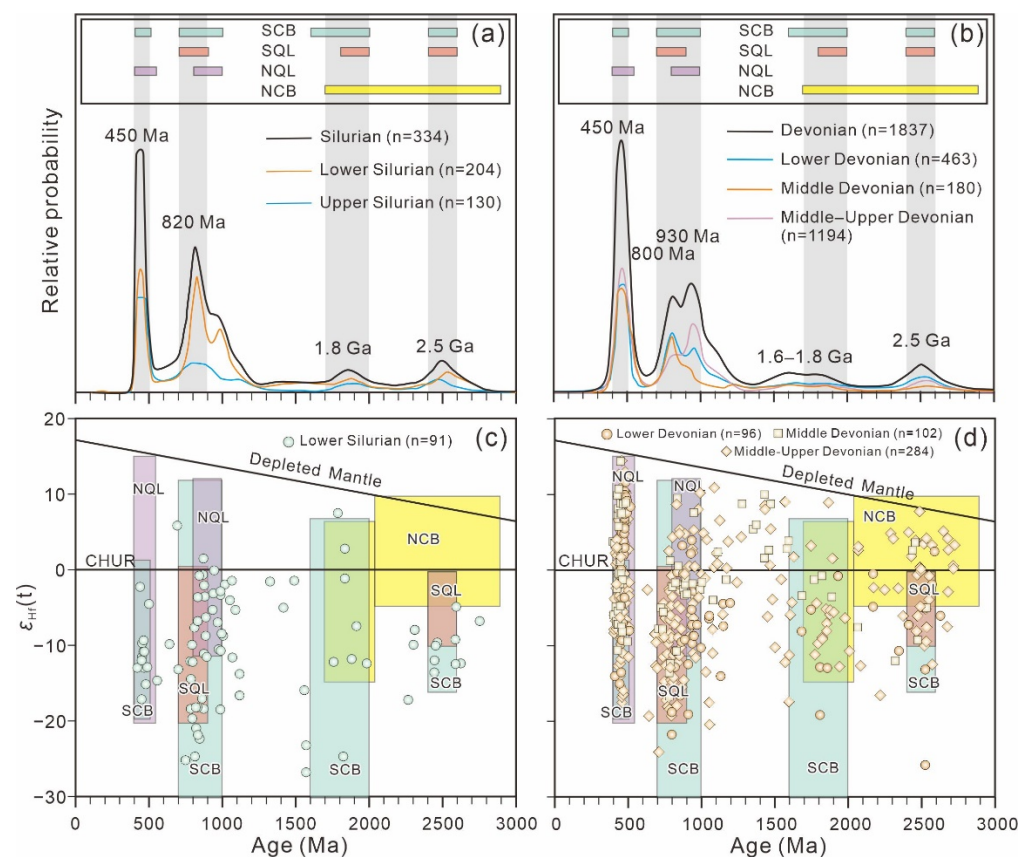


**Figure 11.** Detrital zircon U–Pb age spectra and  $\varepsilon_{\text{Hf}(t)}$  values versus U–Pb age diagram from the Phanerozoic strata in the South Qinling Belt and the surrounding potential sources. (a,c) Silurian [52,62,63]; (b,d) Devonian (this study, [8,27,62,64–72]). Data for North China Block, South China Block, North Qinling Belt, and South Qinling Belt are from [27,52–55]. NCB = North China Block, NQB = North Qinling Belt, SQB = South Qinling Belt, SCB = South China Block.

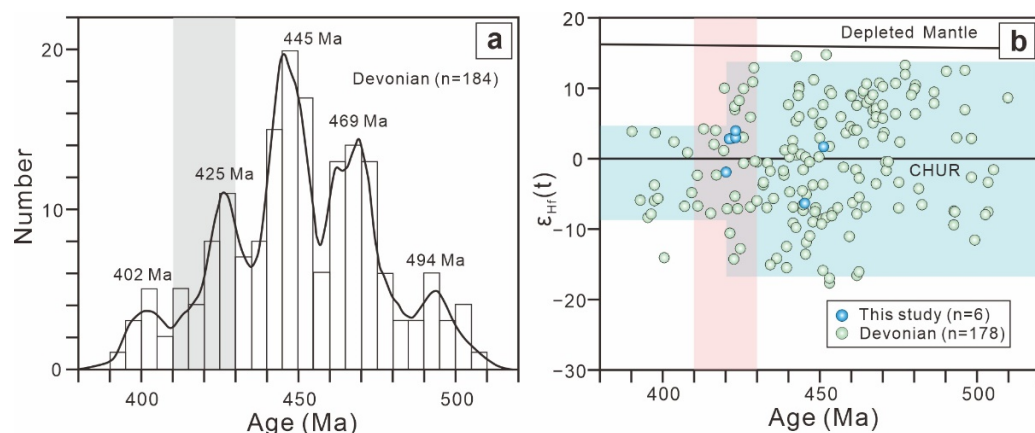


**Figure 12.** (a) Detrital zircon U–Pb age spectra of Phanerozoic detrital zircon grains from Devonian strata. (b) Detrital zircon  $\epsilon_{\text{Hf}(t)}$  values versus U–Pb age diagram of Phanerozoic detrital zircon grains from Devonian strata.

As a result of Shangdan Ocean closure, the clastic sediments from the Devonian should record the tectonic evolution. Therefore, detrital zircon grains that formed during Late Silurian to Early Devonian were selected to investigate the closure process, and the ages and  $\epsilon_{\text{Hf}(t)}$  values are illustrated in Figure 12. These grains show three main populations of 510–475 Ma, 475–420 Ma, and 420–400 Ma (Figure 12a), with  $\epsilon_{\text{Hf}(t)}$  values ranging from  $-11.6$  to  $+13.2$ ,  $-17.7$  to  $+14.7$ , and  $-14.1$  to  $+4.2$ , respectively (Figure 12b). The different age populations are genetically related to the northward subduction of the Shangdan Ocean and the subsequent collision between the North and the South Qinling Belts [3,4,57]. Since the closure time of the Shangdan Ocean spans over a wide period ranging from Late Silurian to Early Devonian, the 430–410 Ma group is further discussed (Figure 12). A remarkable magmatism decrease that appears at ca. 420 Ma (Figure 13a) is due to the collision between the North and South Qinling Belts [17]. The notable shrinking of  $\epsilon_{\text{Hf}(t)}$  values from  $-15.5$ – $+12.8$  to  $-8.4$ – $+4.2$  related to zircon ages ranging from 510–420 Ma to 420–390 Ma, respectively, reflects the change in the relative contributions of the mantle and crustal sources in their genesis [73]. The significant change in the  $\epsilon_{\text{Hf}(t)}$  value at ca. 420 Ma is correlated with plate subduction and collision [16,74–76]. Therefore, the closure of the Shangdan Ocean might have occurred at ca. 420 Ma.

#### 5.4. Tectonic Implications

The Proto-Tethys Ocean was formed during the breakup of Rodinia at ca. 750 Ma [77]. Different parts that split up from Rodinia led to the formation of the South China, North China, Alex, Qaidam, and Tarim Blocks before 550 Ma [1,2]. Several branches of the Proto-Tethys Ocean were formed, including the Shangdan Ocean between the North and South China blocks, the Northern and Southern Qilian Oceans between the Alxa, Central Qilian Terranes, and Qaidam Blocks, and the Kunlun Ocean between the Qaidam, Qiangtang, and Tarim Blocks [2]. Those embranchments opened and subducted during ca. 541–485 Ma [2] and gradually closed in the early Paleozoic (500–420 Ma) [1,2].

The Shangdan Ocean, as the eastmost embranchment of the Proto-Tethys Ocean, is critical for reconstructing the evolution of the Proto-Tethys Ocean [4,56,78]. The subduction-related ophiolitic rocks show that the formation time of the Shangdan Ocean can be constrained at ca. 534–470 Ma [28]. Widely distributed ca. 510–420 Ma arc-magmatism and the formation of the gabbroic and granitic intrusions in the North Qinling Belt suggest northward subduction of the Shangdan Ocean underneath the North Qinling Belt during early Paleozoic (Figure 13a) [3]. In contrast to Silurian strata, these magmatic ages are only found in the Devonian strata of the South Qinling (Figures 11 and 13). Furthermore, a large number of detrital zircon grains at 510–420 Ma also supports this hypothesis (Figure 12). At ca. 420 Ma, the noticeable reduction in magmatism and the change in  $\epsilon_{\text{Hf}(t)}$  values of

the detrital zircons from the Devonian strata in the South Qinling Belt unveil the closure of the Shangdan Ocean as well as the collision between the North and South Qinling Belts (Figure 13b). This is also supported by the metamorphic ages of metamorphic rocks. The amphibolite facies metamorphism of the Qinling Complex is constrained at 420 to 400 Ma, which is correlated to the collision between the North and South Qinling Belts [28,79,80]. The Wushan ductile shear zone as a branch of the Shangdan Suture Zone was intruded by a granitic dyke with the zircon U–Pb age of  $403 \pm 3.5$  Ma, which is regarded as the minimum formation age of the Shangdan Suture Zone [81]. Therefore, the Shangdan Ocean as the eastmost embranchment of the Proto-Tethys Ocean was closed at ca. 420 Ma, and the Shangdan Suture Zone was formed by the collision between the North and the South Qinling Belts (Figure 13b).

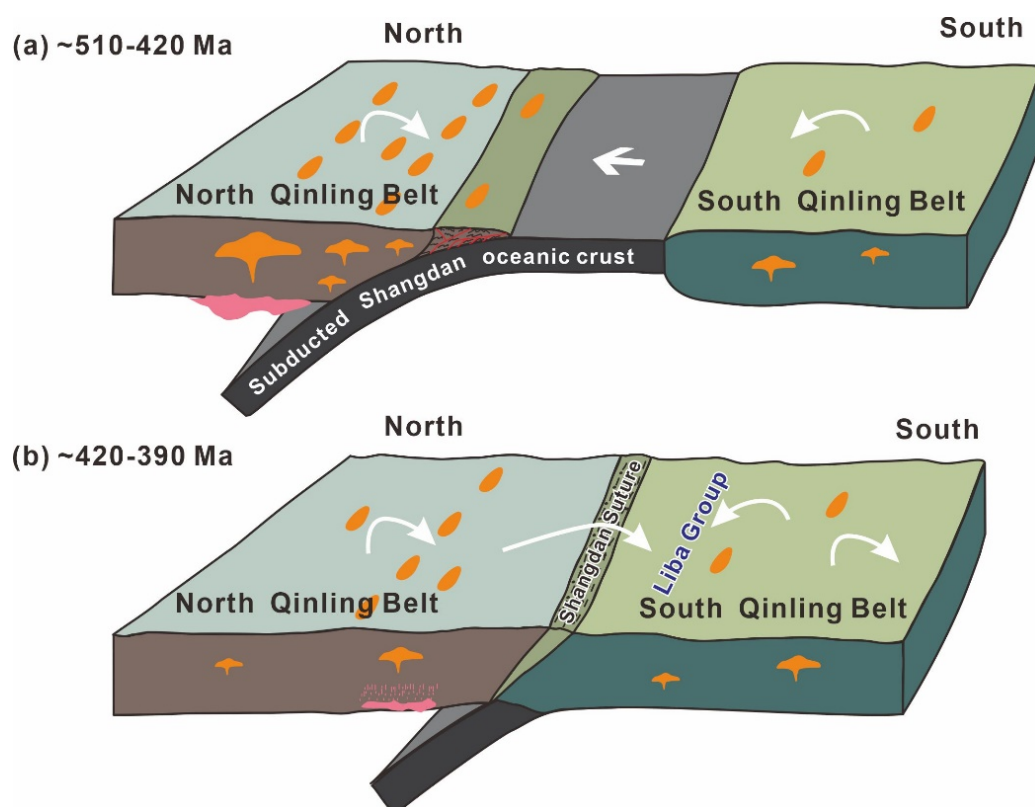


**Figure 13.** Schematic cartoon showing the tectonic evolution of the Shangdan Ocean. (a) Subduction of the Shangdan oceanic slab from 510 to 420 Ma. (b) Collision between the North Qinling Belt and South Qinling Belt at ca. 420 Ma. The white arrows show the transport direction of detrital sediments.

## 6. Conclusions

The maximum deposition age of the Liba Group is constrained at  $418 \pm 13$  Ma, indicating that the strata were deposited during the Middle Devonian. Three age groups and their sources are recognized in the Liba Group, the Phanerozoic detrital zircon grains were sourced from the North Qinling Belt, and the main population represented by Neoproterozoic grains that originated from both the North and South Qinling Belts and the minor Archean–Mesoproterozoic grains came from the North Qinling Belt and the North and South China blocks. Integrated zircon  $\varepsilon_{\text{Hf}(t)}$  values, sedimentary provenance, magmatism, and tectonic setting changes indicate that the Shangdan Ocean as the eastmost embranchment of the Proto-Tethys was closed at ca. 420 Ma.

**Author Contributions:** Conceptualization: S.-S.L.; formal analysis: D.-Y.H. and Q.-S.C.; writing: P.-C.Z.; review and editing: B.L. and G.B.K.; investigation: X.-C.S. All authors have read and agreed to the published version of the manuscript.

**Funding:** This research was funded by the National Natural Science Foundation (42072087), the National Key Research Program (2019YFA0708603), the 111 Project (BP0719021), the Beijing Nova Program (Z201100006820097), and the Chinese Postdoctoral Science Foundation (2021M692995).

**Data Availability Statement:** All the data is presented in the paper.

**Conflicts of Interest:** The authors declare no conflict of interest.

## References

1. Zhao, G.; Wang, Y.; Huang, B.; Dong, Y.; Li, S.; Zhang, G.; Yu, S. Geological reconstructions of the East Asian blocks: From the breakup of Rodinia to the assembly of Pangea. *Earth Sci. Rev.* **2018**, *186*, 262–286. [[CrossRef](#)]
2. Dong, Y.; Sun, S.; Santosh, M.; Zhao, J.; Sun, J.; He, D.; Shi, X.; Hui, B.; Cheng, C.; Zhang, G. Central China Orogenic Belt and amalgamation of East Asian continents. *Gondwana Res.* **2021**, *100*, 131–194. [[CrossRef](#)]
3. Dong, Y.; Santosh, M. Tectonic architecture and multiple orogeny of the Qinling Orogenic Belt, Central China. *Gondwana Res.* **2016**, *29*, 1–40. [[CrossRef](#)]
4. Li, S.; Zhao, S.; Liu, X.; Cao, H.; Yu, S.; Li, X.; Somerville, I.; Yu, S.; Suo, Y. Closure of the Proto-Tethys Ocean and Early Paleozoic amalgamation of microcontinental blocks in East Asia. *Earth Sci. Rev.* **2018**, *186*, 37–75. [[CrossRef](#)]
5. Wang, T.; Wang, X.; Tian, W.; Zhang, C.; Li, W.; Li, S. North Qinling Paleozoic granite associations and their variation in space and time: Implications for orogenic processes in the orogens of central China. *Sci. China Ser. D Earth Sci.* **2009**, *52*, 1359–1384. [[CrossRef](#)]
6. Ren, L.; Liang, H.; Bao, Z.; Zhang, J.; Li, K.; Huang, W. The petrogenesis of early Paleozoic high-Ba–Sr intrusions in the North Qinling terrane, China, and tectonic implications. *Lithos* **2018**, *314–315*, 534–550. [[CrossRef](#)]
7. Zhang, C.; Liu, L.; Wang, T.; Wang, X.; Li, L.; Gong, Q.; Li, X. Granitic magmatism related to early Paleozoic continental collision in North Qinling. *Chin. Sci. Bull.* **2013**, *58*, 4405–4410. [[CrossRef](#)]
8. Dong, Y.; Liu, X.; Neubauer, F.; Zhang, G.; Tao, N.; Zhang, Y.; Zhang, X.; Li, W. Timing of Paleozoic amalgamation between the North China and South China Blocks: Evidence from detrital zircon U–Pb ages. *Tectonophysics* **2013**, *586*, 173–191. [[CrossRef](#)]
9. Qin, Z.; Wu, Y.; Siebel, W.; Gao, S.; Wang, H.; Abdallsamed, M.I.M.; Zhang, W.; Yang, S. Genesis of adakitic granitoids by partial melting of thickened lower crust and its implications for early crustal growth: A case study from the Huichizi pluton, Qinling orogen, central China. *Lithos* **2015**, *238*, 1–12. [[CrossRef](#)]
10. Chang, H.; Wu, Y.; Zhou, G.; Zhang, W.; He, Y.; Yujie, Z.; Hu, P.; Hu, Z. Zircon U–Pb geochronology and geochemistry of the Lajimiao mafic complex in the Shangdan Suture Zone, Qinling orogen: Petrogenesis and tectonic implications. *Lithos* **2021**, *390–391*, 106113. [[CrossRef](#)]
11. Gehrels, G. Detrital Zircon U–Pb Geochronology Applied to Tectonics. *Annu. Rev. Earth Planet. Sci.* **2014**, *42*, 127–149. [[CrossRef](#)]
12. Fedo, C.M. Detrital Zircon Analysis of the Sedimentary Record. *Rev. Mineral. Geochem.* **2003**, *53*, 277–303. [[CrossRef](#)]
13. Nelson, D.R. An assessment of the determination of depositional ages for precambrian clastic sedimentary rocks by U–Pb dating of detrital zircons. *Sediment. Geol.* **2001**, *141*, 37–60. [[CrossRef](#)]
14. Dickinson, W.R.; Gehrels, G.E. Use of U–Pb ages of detrital zircons to infer maximum depositional ages of strata: A test against a Colorado Plateau Mesozoic database. *Earth Planet. Sci. Lett.* **2009**, *288*, 115–125. [[CrossRef](#)]
15. Zhang, J.Y.; Wang, Q.; Liu, X.F.; Zhou, G.F.; Xu, H.P.; Zhu, Y.G. Provenance and ore-forming process of Permian lithium-rich bauxite in central Yunnan, SW China. *Ore Geol. Rev.* **2022**, *145*, 104862. [[CrossRef](#)]
16. Spencer, C.J.; Kirkland, C.L.; Prave, A.R.; Strachan, R.A.; Pease, V. Crustal reworking and orogenic styles inferred from zircon Hf isotopes: Proterozoic examples from the North Atlantic region. *Geosci. Front.* **2019**, *10*, 417–424. [[CrossRef](#)]
17. Cawood, P.A.; Hawkesworth, C.J.; Dhuime, B. Detrital zircon record and tectonic setting. *Geology* **2012**, *40*, 875–878. [[CrossRef](#)]
18. Yu, H.C.; Qiu, K.F.; Pirajno, F.; Zhang, P.C.; Dong, W.Q. Revisiting Phanerozoic evolution of the Qinling Orogen (East Tethys) with perspectives of detrital zircon. *Gondwana Res.* **2022**, *103*, 426–444. [[CrossRef](#)]
19. Qiu, K.; Yu, H.; Deng, J.; McIntire, D.; Gou, Z.; Geng, J.; Chang, Z.; Zhu, R.; Li, K.; Goldfarb, R. The giant Zaozigou Au–Sb deposit in West Qinling, China: Magmatic- or metamorphic-hydrothermal origin? *Mineral. Deposita* **2020**, *55*, 345–362. [[CrossRef](#)]
20. Goldfarb, R.J.; Mao, J.W.; Qiu, K.F.; Goryachev, N. The great Yanshanian metallogenic event of eastern Asia: Consequences from one hundred million years of plate margin geodynamics. *Gondwana Res.* **2021**, *100*, 223–250. [[CrossRef](#)]
21. Qiu, K.F.; Deng, J.; Yu, H.C.; Wu, M.Q.; Wang, Y.; Zhang, L.; Goldfarb, R. Identifying hydrothermal quartz vein generations in the Taiyangshan porphyry Cu–Mo deposit (West Qinling, China) using cathodoluminescence, trace element geochemistry, and fluid inclusions. *Ore Geol. Rev.* **2021**, *128*, 103882. [[CrossRef](#)]
22. Qiu, K.F.; Yu, H.C.; Hetherington, C.; Huang, Y.Q.; Yang, T.; Deng, J. Tourmaline composition and boron isotope signature as a tracer of magmatic-hydrothermal processes. *Am. Mineral.* **2021**, *106*, 1033–1044. [[CrossRef](#)]
23. Dong, Y.; Yang, Z.; Liu, X.; Zhang, X.; He, D.; Li, W.; Zhang, F.; Sun, S.; Zhang, H.; Zhang, G. Neoproterozoic amalgamation of the Northern Qinling terrain to the North China Craton: Constraints from geochronology and geochemistry of the Kuanping ophiolite. *Precambrian Res.* **2014**, *255*, 77–95. [[CrossRef](#)]
24. Hu, F.; Liu, S.; Ducea, M.N.; Chapman, J.B.; Wu, F.; Kusky, T. Early Mesozoic magmatism and tectonic evolution of the Qinling Orogen: Implications for oblique continental collision. *Gondwana Res.* **2020**, *88*, 296–332. [[CrossRef](#)]

25. Yu, S.; Li, S.; Zhang, J.; Peng, Y.; Somerville, I.; Liu, Y.; Wang, Z.; Li, Z.; Yao, Y.; Li, Y. Multistage anatexis during tectonic evolution from oceanic subduction to continental collision: A review of the North Qaidam UHP Belt, NW China. *Earth Sci. Rev.* **2019**, *191*, 190–211. [[CrossRef](#)]
26. Dong, Y.; Zhang, G.; Hauzenberger, C.; Neubauer, F.; Yang, Z.; Liu, X. Palaeozoic tectonics and evolutionary history of the Qinling orogen: Evidence from geochemistry and geochronology of ophiolite and related volcanic rocks. *Lithos* **2011**, *122*, 39–56. [[CrossRef](#)]
27. Liao, X.; Wang, Y.; Liu, L.; Wang, C.; Santosh, M. Detrital zircon U-Pb and Hf isotopic data from the Liuling Group in the South Qinling belt: Provenance and tectonic implications. *J. Asian Earth Sci.* **2017**, *134*, 244–261. [[CrossRef](#)]
28. Dong, Y.; Zhang, G.; Neubauer, F.; Liu, X.; Genser, J.; Hauzenberger, C. Tectonic evolution of the Qinling orogen, China: Review and synthesis. *J. Asian Earth Sci.* **2011**, *41*, 213–237. [[CrossRef](#)]
29. Yu, H.C.; Qiu, K.F.; Hetherington, C.J.; Chew, D.; Huang, Y.Q.; He, D.Y.; Geng, J.Z.; Xian, H.Y. Apatite as an alternative petrochronometer to trace the evolution of magmatic systems containing metamict zircon. *Contrib. Mineral. Petrol.* **2021**, *176*, 1–19. [[CrossRef](#)]
30. Zhang, L.; Qiu, K.; Hou, Z.; Pirajno, F.; Shivute, E.; Cai, Y. Fluid-rock reactions of the Triassic Taiyangshan porphyry Cu-Mo deposit (West Qinling, China) constrained by QEMSCAN and iron isotope. *Ore Geol. Rev.* **2021**, *132*, 104068. [[CrossRef](#)]
31. Ke, C.; Wand, X.; Nie, Z.; Yang, Y.; Lü, X.; Wang, S.A.; Li, J. Age, geochemistry, Nd-Hf isotopes and relationship between granite and gold mineralization of Zhongchuan granitoid pluton in West Qinling. *Chin. Geol.* **2020**, *47*, 1127–1154.
32. Zeng, Q.; McCuaig, T.C.; Hart, C.J.R.; Jourdan, F.; Muhling, J.; Bagas, L. Structural and geochronological studies on the Liba goldfield of the West Qinling Orogen, Central China. *Mineral. Deposita* **2012**, *47*, 799–819. [[CrossRef](#)]
33. Yu, H.C.; Qiu, K.F.; Nassif, M.T.; Geng, J.Z.; Sai, S.X.; Duo, D.W.; Huang, Y.Q.; Wang, J. Early orogenic gold mineralization event in the West Qinling related to closure of the Paleo-Tethys Ocean—Constraints from the Ludousou gold deposit, central China. *Ore Geol. Rev.* **2020**, *117*, 103217. [[CrossRef](#)]
34. He, D.Y.; Qiu, K.F.; Santosh, M.; Yu, H.C.; Long, Z.Y.; Wang, J.Y. Inhomogeneous crust-mantle interaction and Triassic tectonic escape of a Proterozoic microplate: A tale of the Bikou Terrane. *Lithos* **2021**, *396*, 106227. [[CrossRef](#)]
35. Qiu, K.F.; Yu, H.C.; Gou, Z.Y.; Liang, Z.L.; Zhang, J.L.; Zhu, R. Nature and origin of Triassic igneous activity in the Western Qinling Orogen: The Wenquan composite pluton example. *Int. Geol. Rev.* **2018**, *60*, 242–266. [[CrossRef](#)]
36. Sun, S.; Song, C.; Wu, A.; Yuan, M.; Gao, B. Geochemical characteristics of gold-bearing turbidite formation in Liba Group of Limin gold deposit, West Qinling. *Acta Sediment. Sin.* **1995**, *13*, 145–152.
37. Shi, J. *Geological Detailed Investigation Report of 87 and 135 Section Lines in the Zhaogou Gold Deposit*; Geological Team under Gansu Geological Survey Internal: Lanzhou, China, 2000; pp. 1–80.
38. Geng, J.; Qiu, K.; Gou, Z.; Yu, H. Tectonic regime switchover of Triassic Western Qinling Orogen: Constraints from LA-ICP-MS zircon U–Pb geochronology and Lu–Hf isotope of Dangchuan intrusive complex in Gansu, China. *Geochemistry* **2017**, *77*, 637–651. [[CrossRef](#)]
39. Qiu, K.; Yu, H.; Wu, M.; Geng, J.; Ge, X.; Gou, Z.; Taylor, R.D. Discrete Zr and REE mineralization of the Baerzhe rare-metal deposit, China. *Am. Mineral.* **2019**, *104*, 1487–1502. [[CrossRef](#)]
40. Andersen, T. Correction of common lead in U–Pb analyses that do not report <sup>204</sup>Pb. *Chem. Geol.* **2002**, *192*, 59–79. [[CrossRef](#)]
41. Wiedenbeck, M.; Alle, P.; Corfu, F.; Griffin, W.; Meier, M.; Oberli, F.V.; Quadt, A.V.; Roddick, J.; Spiegel, W. Three natural zircon standards for U–Th–Pb, Lu–Hf, trace element and REE analyses. *Geostand. Newslett.* **1995**, *19*, 1–23. [[CrossRef](#)]
42. Sláma, J.; Košler, J.; Condon, D.J.; Crowley, J.L.; Gerdes, A.; Hanchar, J.M.; Horstwood, M.S.A.; Morris, G.A.; Nasdala, L.; Norberg, N.; et al. Plešovice zircon—A new natural reference material for U–Pb and Hf isotopic microanalysis. *Chem. Geol.* **2008**, *249*, 1–35. [[CrossRef](#)]
43. Vermeesch, P. On the visualisation of detrital age distributions. *Chem. Geol.* **2012**, *312–313*, 190–194. [[CrossRef](#)]
44. Ludwig, K. *Isoplot 4.15: A Geochronological Toolkit for Microsoft Excel*; Berkeley Geochronological Center: Berkeley, CA, USA, 2012; p. 5.
45. Gehrels, G.; Valencia, V.; Pullen, A.J. Detrital zircon geochronology by laser-ablation multicollector ICPMS at the Arizona LaserChron Center. *Paleontol. Soc. Pap.* **2006**, *12*, 67–76. [[CrossRef](#)]
46. Elhlou, S.; Belousova, E.; Griffin, W.L.; Pearson, N.J.; O’Reilly, S.Y. Trace element and isotopic composition of GJ-red zircon standard by laser ablation. *Geochim. Cosmochim. Acta* **2006**, *70*, 158. [[CrossRef](#)]
47. Kinny, P.D.; Wijbrans, J.R.; Froude, D.O.; Williams, I.S.; Compston, W. Age constraints on the geological evolution of the Narryer Gneiss Complex, Western Australia. *Aust. J. Earth Sci.* **1990**, *37*, 51–69. [[CrossRef](#)]
48. Wu, Y.; Zheng, Y. Zircon genetic mineralogy and its constraints on U–Pb age interpretation. *Chin. Sci. Bull.* **2004**, *49*, 1589–1604. [[CrossRef](#)]
49. Li, J.S.; Chun, H.; Wu, A.; Yuan, M.; Gao, B. Stratigraphy disintegration of shujiaba Formation and its vertical transport model of turbidity current in Liba Group, West Qinling mountains. *Acta Geol. Gansu* **1996**, *5*, 33–40.
50. Li, Y.; Jin, H. Trace fossils of devonian system in northern belt of west Qinling and their environmental significance. *Chin. Sci* **1993**, *23*, 1322–1330.
51. Ye, X. On the occurrence of spore assemblages from the Shujiaba Region of Tianshui County, Gansu and their stratigraphical significance. *Northwest Geosci.* **1986**, *13*, 89–101.

52. Chen, W.; Pei, X.; Liu, C.; Li, R.; Li, Z.; Wei, B.; Xu, X.; Liu, T.; Wang, Y.; Ren, H. U-Pb ages of detrital zircons from Taiyangsi Rock Group in Shujiaba area of West Qinling Mountains and their geological significance. *Chin. Geol.* **2014**, *41*, 741–755.
53. Shi, Y.; Yu, J.; Santosh, M. Tectonic evolution of the Qinling orogenic belt, Central China: New evidence from geochemical, zircon U–Pb geochronology and Hf isotopes. *Precambrian Res.* **2013**, *231*, 19–60. [[CrossRef](#)]
54. Xia, X.; Sun, M.; Zhao, G.; Wu, F.; Xu, P.; Zhang, J.; Luo, Y. U–Pb and Hf isotopic study of detrital zircons from the Wulashan khondalites: Constraints on the evolution of the Ordos Terrane, Western Block of the North China Craton. *Earth Planet. Sci. Lett.* **2006**, *241*, 581–593. [[CrossRef](#)]
55. Chen, Q.; Sun, M.; Long, X.; Zhao, G.; Wang, J.; Yu, Y.; Yuan, C. Provenance study for the Paleozoic sedimentary rocks from the west Yangtze Block: Constraint on possible link of South China to the Gondwana supercontinent reconstruction. *Precambrian Res.* **2018**, *309*, 271–289. [[CrossRef](#)]
56. Wu, Y.; Zheng, Y. Tectonic evolution of a composite collision orogen: An overview on the Qinling–Tongbai–Hong’an–Dabie–Sulu orogenic belt in central China. *Gondwana Res.* **2013**, *23*, 1402–1428. [[CrossRef](#)]
57. Wang, X.; Wang, T.; Zhang, C. Neoproterozoic, Paleozoic, and Mesozoic granitoid magmatism in the Qinling Orogen, China: Constraints on orogenic process. *J. Asian Earth Sci.* **2013**, *72*, 129–151. [[CrossRef](#)]
58. Santosh, M.; Liu, D.; Shi, Y.; Liu, S.J. Paleoproterozoic accretionary orogenesis in the North China Craton: A SHRIMP zircon study. *Precambrian Res.* **2013**, *227*, 29–54. [[CrossRef](#)]
59. Santosh, M.; Sajeev, K.; Li, J.H. Extreme crustal metamorphism during Columbia supercontinent assembly: Evidence from North China Craton. *Gondwana Res.* **2006**, *10*, 256–266. [[CrossRef](#)]
60. Sun, J.; Dong, Y. Stratigraphy and geochronology of Permo–Carboniferous strata in the Western North China Craton: Insights into the tectonic evolution of the southern Paleo-Asian Ocean. *Gondwana Res.* **2020**, *88*, 201–219. [[CrossRef](#)]
61. Wu, F.; Zhang, Y.; Yang, J.; Xie, L.; Yang, Y. Zircon U–Pb and Hf isotopic constraints on the Early Archean crustal evolution in Anshan of the North China Craton. *Precambrian Res.* **2008**, *167*, 339–362. [[CrossRef](#)]
62. Duan, L. Detrital Zircon Provenance of the Silurian and Devonian in South Qingling, and the Northwestern Margin of Yangtze Terrane and Its Tectonic Implications. *Xi’an Northwest Univ.* **2010**, *1*, 67.
63. Liu, T.; Pei, X.; Liu, C.; Li, Z.; Li, R.; Wei, B.; Wang, Y.; Ren, H.; Xu, X.; Chen, W. LA-ICP-MS U-Pb ages of detrital zircons from the Yangyangsiyan Formation in Liangdang area, Western Qinling: Age and provenance characteristics. *Geol. Bull. China* **2014**, *33*, 1028–1040.
64. Ding, Z.; Wen, C.; Guo, A.; Niu, G.; Wang, Z.; Liu, Z. Stratigraphic age and provenance characteristics of the Wujiashan Group in the West Qinling Mountains: Evidence from detrital zircon U-Pb age. *J. Earth Sci. Environ* **2018**, *40*, 111–132.
65. Yan, Z.; Aitchison, J.C.; Fu, C.; Guo, X.; Xia, W.; Niu, M. Devonian sedimentation in the Xiqingshan Mountains: Implications for paleogeographic reconstructions of the SW Qinling Orogen. *Sediment. Geol.* **2016**, *343*, 1–17. [[CrossRef](#)]
66. Li, Z. *Research on Detrital Zircons from the Devonian Clastic Sequence in the South Qinling Belt and the Late Neoproterozoic to Early Paleozoic Sedimentary Rocks at the Northern Margin of the Yangtze Block and Its Geological Significance*; Northwest University: Xi’an, China, 2019.
67. Gao, F.; Pei, X.; Li, R.; Li, Z.; Pei, L.; Chen, Y.; Wang, M.; Liu, C.; Li, Z. Detrital zircon U-Pb ages of the Liuling Group in shangdan area, Eastern Qinling Mountains and their geological significance. *Earth Sci.* **2019**, *44*, 2519–2535.
68. Gao, X. *Geological Features and Geological Significance of Late Paleozoic Depositional Stratum in the Lintan Area of the West Qinling Orogen*; Chang’an University: Xi’an, China, 2019.
69. Wang, Y.; Pei, X.; Liu, C.; Li, R.; Li, Z.; Wei, B.; Ren, H.; Chen, W.; Liu, T.; Xu, X. LA-ICP-MS U-Pb age of detrital zircons from devonian Shujiaba Group in the Shujiaba area, Western Qinling: Provenance characteristics and formation age. *Geol. Bull. China* **2014**, *33*, 1015–1027.
70. Wu, S.; Pei, X.; Li, Z.; Li, R.; Pei, L.; Chen, Y.; Gao, J.; Liu, C.; Wei, F.; Wang, Y. Provenance of dacaoan Group in the northern margin of west Qinling Orogenic Belt: LA-ICP-MS Detrital zircon U-Pb age evidence. *Geol. Bull. China* **2012**, *31*, 1469–1481.
71. Ji, X.; Yang, L.; Santosh, M.; Li, N.; Zhang, C.; Zhang, Z.; Han, R.; Li, Z.; Wu, C. Detrital zircon geochronology of Devonian quartzite from tectonic mélange in the Mianlue Suture Zone, Central China: Provenance and tectonic implications. *Int. Geol. Rev.* **2016**, *58*, 1510–1527. [[CrossRef](#)]
72. Yang, L.Q.; Ji, X.Z.; Santosh, M.; Li, N.; Zhang, Z.C.; Yu, J.Y. Detrital zircon U–Pb ages, Hf isotope, and geochemistry of Devonian chert from the Mianlue suture: Implications for tectonic evolution of the Qinling orogen. *J. Asian Earth Sci.* **2015**, *113*, 589–609. [[CrossRef](#)]
73. Goodge, J.W.; Vervoort, J.D. Origin of Mesoproterozoic A-type granites in Laurentia: Hf isotope evidence. *Earth Planet. Sci. Lett.* **2006**, *243*, 711–731. [[CrossRef](#)]
74. Bruno, H.; Heilbron, M.; Strachan, R.; Fowler, M.; de Morisson Valeriano, C.; Bersan, S.; Moreira, H.; Cutts, K.; Dunlop, J.; Almeida, R.; et al. Earth’s new tectonic regime at the dawn of the Paleoproterozoic: Hf isotope evidence for efficient crustal growth and reworking in the São Francisco craton, Brazil. *Geology* **2021**, *49*, 1214–1219. [[CrossRef](#)]
75. Kemp, A.I.S.; Hawkesworth, C.J.; Foster, G.L.; Paterson, B.A.; Woodhead, J.D.; Hergt, J.M.; Gray, C.M.; Whitehouse, M.J. Magmatic and Crustal Differentiation History of Granitic Rocks from Hf–O Isotopes in Zircon. *Science* **2007**, *315*, 980–983. [[CrossRef](#)] [[PubMed](#)]
76. Laurent, O.; Zeh, A. A linear Hf isotope-age array despite different granitoid sources and complex Archean geodynamics: Example from the Pietersburg block (South Africa). *Earth Planet. Sci. Lett.* **2015**, *430*, 326–338. [[CrossRef](#)]

77. Cawood, P.A.; McCausland, P.J.; Dunning, G.R. Opening Iapetus: Constraints from the Laurentian margin in Newfoundland. *Geol. Soc. Am. Bull.* **2001**, *113*, 443–453. [[CrossRef](#)]
78. Song, S.; Niu, Y.; Su, L.; Xia, X. Tectonics of the North Qilian orogen, NW China. *Gondwana Res.* **2013**, *23*, 1378–1401. [[CrossRef](#)]
79. Liu, L.; Liao, X.; Wang, Y.; Wang, C.; Santosh, M.; Yang, M.; Zhang, C.; Chen, D. Early Paleozoic tectonic evolution of the North Qinling Orogenic Belt in Central China: Insights on continental deep subduction and multiphase exhumation. *Earth Sci. Rev.* **2016**, *159*, 58–81. [[CrossRef](#)]
80. Diwu, C.; Sun, Y.; Zhao, Y.; Liu, B.; Lai, S. Geochronological, geochemical, and Nd-Hf isotopic studies of the Qinling Complex, central China: Implications for the evolutionary history of the North Qinling Orogenic Belt. *Geosci. Front.* **2014**, *5*, 499–513. [[CrossRef](#)]
81. Liang, X.; Sun, S.; Dong, Y.; Yang, Z.; Liu, X.; He, D. Fabrics and geochronology of the Wushan ductile shear zone: Tectonic implications for the Shangdan suture zone in the Qinling orogen, Central China. *J. Asian Earth Sci.* **2017**, *139*, 71–82. [[CrossRef](#)]